Author Manuscript

Author Manuscript

Author Manuscript

Author Manuscript

HHS Public Access

Author manuscript

Med Devices Sens. Author manuscript; available in PMC 2022 July 01.

Published in final edited form as:

Med Devices Sens. 2019 April ; 2(2): . doi:10.1002/mds3.10032.

Silicon nitride enhances osteoprogenitor cell growth and differentiation via increased surface energy and formation of amide and nanocrystalline HA for craniofacial reconstruction

Kamal R. Awad[1,2], **Neelam Ahuja**[3], **Ami Shah**[1], **Henry Tran**[3], **Pranesh B. Aswath**[1], **Marco Brotto**[3], **Venu Varanasi**[1,3]

[1]Department of Material Science and Engineering, University of Texas at Arlington, Arlington, Texas

[2]Department of Refractories and Ceramics, National Research Centre, Giza, Egypt

[3]College of Nursing & Health Innovation, University of Texas at Arlington, Arlington, Texas

Abstract

The bioactive silicon nitride (Si_3N_4) has been FDA cleared for use as spinal intervertebral arthrodesis devices. Because its surface properties promote bone ongrowth and ingrowth, it also has the potential to benefit craniofacial reconstruction. Thus, the aim of this work was to determine whether the surface properties of Si_3N_4 could enhance the osteoblast cell growth, differentiation and nucleation of hydroxyapatite (HA) crystals compared to conventional implant materials such as titanium (Ti) and polyether ether ketone (PEEK). X-ray absorbance near-edge structure analysis (XANES) indicated the presence of Si-Si, Si-O and Si-N bonding. Surface wettability studies confirmed that Si_3N_4 exhibits the lowest contact angle and highest surface energy. Cell culture studies showed that osteoblast growth was enhanced on Si_3N_4 after 1 day and up to 7 days. Si_3N_4 surface induced highest surface coverage and thickness of nanocrystalline HA (211) and (203) in cell-free in vitro studies after 7 days of culture. Raman spectroscopy analysis confirmed the presence of surface functional groups consisting of phosphate and carbonate species. Interestingly, Si_3N_4 surface showed amide and hydroxyproline groups, the precursors to collagen, which were not observed on Ti and PEEK surfaces. Furthermore, Si_3N_4 surface indicated high expression of RUNX2, enhanced cell differentiation and dense collagenous ECM after 30 days of the in vitro study. The present study concluded that Si_3N_4 surface enhances osteoprogenitor cell adhesion, growth, RUNX2 expression and ECM formation via the coupled effects of higher surface energy and the presence of amide and nanocrystalline HA functional groups.

Keywords

amide surface formation; craniofacial implants; hydroxyapatite nucleation; hydroxyproline; silicon nitride

Correspondence Venu Varanasi, Department of Material Science and Engineering, University of Texas at Arlington, Arlington, TX. venu.varanasi@uta.edu.
Kamal R. Awad and Neelam Ahuja are co-first author.

Author Manuscript Author Manuscript Author Manuscript Author Manuscript

1 | INTRODUCTION

Nearly 600,000 bone grafting procedures are performed in the United States and 4 million globally every year at a cost of approximately $2.3 billion annually; this healthcare burden is projected to reach $3.4 billion in 2023 (Transparency Market Research, 2016). Of greater concern is that the number of these procedures is estimated to rise 400% by 2050 as a result of increases in both population and life expectancy (National Center for Health Statistics, 2006). Craniofacial reconstructive procedures are often required for facial trauma, tumour resection, for congenital and birth defects. These reconstructive procedures require the use of implants made of autologous and heterologous bone grafts, or abiotic biomaterials. Autograft, allograft and some biomaterials provide good biomimetic properties whereas others, like titanium, have higher primary tear resistance (Zanotti et al., 2016). The use of autologous bone grafts for repair and regeneration of critical-sized defects (CSD) is not feasible and difficult due to the 3-dimensional complexity of structures, limited secondary site volumes along with donor site comorbidities. Bioceramics such as hydroxyapatite (HA) are used clinically for bone repair and reconstruction, and their ability to promote bone integration by rapid cellular proliferation makes them suitable for limited reconstruction (Dorozhkin, 2015). However, HA's fragile nature, lack of osteosynthesis capacity (Itoh et al., 2002), risk of secondary infections (Laure et al., 2008) (especially in frontal sinus, orbital and paranasal regions) and lack of long-term stability make it unfavourable for long-term craniofacial implants (Itoh et al., 2002; Lazarinis et al., 2017). Multiple studies have documented poor healing of CSD traumatic fractures for patients receiving standard-of-care medical treatments. Large gaps of missing bone in CSDs require fixative implants to provide structure and strength for load-bearing applications (Turk et al., 2004). Consequently, various implant materials such as PEEK and Ti are widely employed for craniofacial reconstruction.

Polyether ether ketone is used in a number of orthopaedic applications including trauma, arthroplasty and spinal fusion because of its biocompatibility, inert nature and low elastic modulus (Kurtz & Devine, 2007). PEEK's modulus is designed to mimic bone, and therefore, it minimizes stress shielding when compared to Ti (Rao, Pelletier, Walsh, & Mobbs, 2014; Steinberg et al., 2013). Yet, PEEK's fundamental flaw is its lack of bioactivity which precludes any adequate biological or mechanical integration with bone. Its low surface energy, smoothness and poor wettability limit osteoblastic differentiation and bone regeneration when compared to Ti (Olivares Navarrete et al., (2012); Pelletier et al., 2016). Surface modifications and coatings (e.g., HA and tri-calcium phosphate [β-TCP]), as well as plasma treatments, help facilitate cell adhesion, differentiation and overall integration with bone (Kurtz & Devine, 2007; Webster, Patel, Rahaman, & Sonny Bal, 2012). These coatings increase surface bioactivity but at the expense of reduced strength, particularly in the case of HA (Abu Bakar et al., 2003; Petrovic et al., 2006), and reduced cellular growth for β-TCP (Petrovic et al., 2006). These types of coatings show low bonding to PEEK, leading to poor interfacial interaction and delamination (Abu Bakar et al., 2003). Although they are still under development, coated PEEK is less than ideal as a fixative implant material.

Titanium and its alloys are biocompatible and have an inherent ability to osteointegration. They have been widely used in orthopaedic, dental, skeletal and craniofacial reconstruction

Author Manuscript Author Manuscript Author Manuscript Author Manuscript

for many decades (Dabrowski, Swieszkowski, Godlinski, & Kurzydlowski, 2010; Webster et al., 2012). Calcium phosphate coatings on Ti surfaces help increase its bioactivity and osteointegration (Kulkarni Aranya et al., 2017; Lee et al., 2016). However, complications, such as post-implant fractures due to stress shielding, aseptic loosening (Jokstad, 2004; MacInnes, Gordon, & Wilkinson, 2012), poor long-term stability, absence of antioxidant effects (Iwai-Yoshida et al., 2012) and prolonged healing, remain as critical issues. To improve outcomes of fracture repairs using Ti implants, HA coatings have been attempted (Jones, Saigusa, Sickels, Tiner, & Gardner, 1997; Teraoka et al., 2000). However, these coatings proved to be unsatisfactory due to the thermal expansion mismatch at the Ti-HA interface (Hayashi, Matsuguchi, Uenoyama, Kanemaru, & Sugioka, 1989; Klein, Patka, Lubbe, Wolke, & Groot, 1991), the poor quality of HA formed by plasma spraying (Chou & Chang, 1999; Filiaggi, Pilliar, & Coombs, 1993) and poor long-term stability. Bioglass®, an alternative to HA, is also a mechanically weak biomaterial (Braem et al., 2012; Lusquiños et al., 2014). It similarly exhibits cracking at the Ti-glass interface due to its brittleness and thermal expansion mismatch (Bloyer et al., 1999). Additionally, composite coatings, based on HA and Bioglass®, demonstrated immature bone healing and fibrous tissue attachment after 12-week in vivo (Oirschot et al., 2014). Although MgO or N_2-annealing reduced their thermal expansion mismatch and interfacial adhesion (Gomez Vega, Saiz, Tomsia, Marshall, & Marshall, 2000; Oku et al., 2001), these glasses and composites had reduced bioactivity due to the release of Mg^{2+} ions that down-regulated osteogenic markers (Saffarian Tousi et al., 2013). Antibiotics (Zhao, Chu, Zhang, & Wu, 2009) and coatings such as silver (Song, Ryu, & Hong, 2009), zinc (Chou, LeGeros, Chen, & Li, 2007), copper (Zhao et al., 2009) and fluoride (Liu et al., 2008) have been used to incorporate antibacterial effects on Ti surfaces to overcome secondary infections (Kulkarni Aranya et al., 2017). Yet, antibacterial coatings do not induce a more rapid osteoblast and bone growth response, which is needed for long-term osteointegration. Overall, the use of monolithic or coated PEEK and Ti implants for craniofacial reconstruction and orthopaedic applications is still less than optimal for bone healing. Therefore, using an implant material with a surface that induces rapid osteoprogenitor growth is desirable.

Silicon nitride (Si_3N_4) is a novel biomaterial that has shown improved cyto-compatibility and biomineralization versus traditional hydroxyapatite (Pezzotti, McEntire, Bock, Boffelli, et al., 2016; Pezzotti, McEntire, Bock, Zhu, et al., 2016). It was cleared by the FDA for use in spinal fusion procedures in 2008 and serves as intervertebral spacers for stabilization of cervical and thoracolumbar spine. Studies have also been conducted on the development of Si_3N_4 for reconstructive applications (McEntire et al., 2016). Si_3N_4 ceramics have high strength and fracture toughness, inherent phase stability, high wear resistance, low coefficients of friction, hydrophilicity and biocompatibility (Pezzotti et al., 2017). These traits make it a material of interest for craniofacial and dental applications (Bal & Rahaman, 2012; Mazzocchi, Bellosi, & On, 2008). Studies have also shown that Si_3N_4 is anti-infective and enhances osteogenic differentiation of mesenchymal and osteoblast cells when compared to Ti and PEEK (Bal & Rahaman, 2012; Bock et al., 2017; Gorth et al., 2012; Pezzotti, McEntire, Bock, Zhu, et al., 2016; Webster et al., 2012). Chemical modifications to the surface of Si_3N_4 enhanced its biomineralization relative to HA and other competitive biomaterials (Bock, 2018). This was attributed to many factors, including

Author Manuscript Author Manuscript Author Manuscript Author Manuscript

its surface chemistry, hydrophilicity and its strong electronegative surface sites, which promoted cell attachment and migration when compared to HA, Ti or PEEK (Bock et al., 2015; Pezzotti et al., 2017; Pezzotti, McEntire, Bock, Zhu, et al.,2016). Based on prior work with amorphous silicon nitride (Ilyas, Lavrik, Kim, Aswath, & Varanasi, 2015), the presence of surface nitrogen induces the formation of N-H moieties that act as precursors to the amide groups present in collagenous extracellular matrix (ECM). These moieties (e.g., Si-N or N-H bonding) in amorphous silicon nitride (index of refraction = 2.02) elevated specific expression of runt-related transcription factor 2 (RUNX2), a key transcription factor involved in rapid regeneration of new bone, by nearly 2.5-fold versus control-treated samples (Ilyas et al., 2016). This study will seek to determine whether such functional group formation occurs on monolithic ceramic surfaces and if such functional groups enhance osteogenic responses by osteoblasts in this study.

Thus, it is hypothesized that Si_3N_4 enhances osteoprogenitor cell adhesion, growth, RUNX2 expression and ECM deposition via higher surface energy and the presence of amide surface functional groups. The aim of this study was to correlate osteoprogenitor adhesion, growth and differentiation to surface roughness, surface energy and surface functional group formation in order to identify differences in the osteogenic potential of each implant material.

2 | MATERIALS AND METHODS

2.1 | Study design

The surface properties (roughness, energy and functional groups) of each material before and after cell-free in vitro immersion were analysed at the Center for Characterization of Materials and Biology at the University of Texas at Arlington (CCMB, UTA). Methods used to determine surface roughness included atomic force microscopy (AFM), contact and non-contact surface profilometry. Contact angles of two different liquids were measured using sessile drop methods; the collected data were used for the surface energy calculations. In vitro cell-free study using alpha minimum essential medium (α-MEM) was conducted to study biomineral formation on the surface. All samples were immersed in α-MEM and incubated at 37°C in a humidified 5% carbon dioxide (CO_2) atmosphere for 1, 4, and 7 days. Surface functional group formation and biomineral characterization were investigated using Raman spectroscopy, Fourier transform infrared spectroscopy (FT-IR) analysis, high-resolution scanning electron microscopy (HR-SEM) and electron dispersive spectroscopy (EDX/EDS). FT-IR and Raman spectroscopy are particularly unique in that these methods can easily obtain the structural groups that represent collagen type I on non-transparent surfaces. Histological evaluation for collagen requires a transparent light path through the material and polarized light microscopy to image the collagen fibres. The samples studied in this work are non-transparent; thus, FT-IR was chosen to chemically identify collagen type I and SEM was used to image the fibre bundles of collagen.

Unique in vitro cell culture testing was conducted using murine calvaria osteoblast cells (MC3T3-E1) seeded onto each material's surface. Imaging of adherent cells and cell growth measurements were conducted using SEM and cell proliferation assays, respectively. Statistical evaluation of the surface property data and in vitro results was used to determine

Author Manuscript Author Manuscript Author Manuscript Author Manuscript

significant differences between groups. These statistical analyses were conducted via analysis of variance (ANOVA) using the general linearized model in SPSS (SPSS software; IBM Corporation). A post hoc Tukey's analysis was used to determine statistical significance between each group. Statistical significance was signified by the following convention: $*p < 0.05$, $**p < 0.01$ and $***p < 0.001$.

2.2 | Sample preparation

Silicon nitride (Si_3N_4) samples were commercially purchased (Amedica Corporation). (Pezzotti, McEntire, Bock, Boffelli, et al., 2016). This bioceramic has a nominal composition of 90 weight % (wt.%) Si_3N_4, 6 wt.% yttrium oxide (yttria, Y_2O_3) and 4 wt.% aluminium oxide (alumina, Al_2O_3). The Y_2O_3 and Al_2O_3 serve as densification additives. From this composition, a quantity of disc samples (Ø12.7 × 2.5 mm) was prepared for characterization and biological testing. They were separated into two groups—as-fired and polished. The as-fired samples had no post-densification treatments whereas the polished samples were abrasively lapped to a near-mirror finish. Dimensionally identical samples were also prepared from PEEK (ASTM D6262, Ketron® PEEK 1000; Quadrant EPP USA, Inc.; distributed by McMaster-Carr,) and a titanium alloy (ASTM F136, Ti6A4V-ELI, distributed by Vincent Metals). The Ti and PEEK samples were also produced in two groups —as-machined and polished—using 600 grit and 2000 grit abrasive lapping, respectively. All samples were prepared at two different levels of roughness in an effort to examine each material's surface morphology with respect to in vitro osteoblast cell adhesion and growth. All samples were cleaned prior to all characterizations. Samples were immersed in 100% ethanol and ultrasonicated for 5 min to remove any possible surface debris. After sonication, samples were allowed to dry and the quick drying of ethanol leads to clean surface before any characterization. Prior to the in vitro studies, samples were gas sterilized using ethylene oxide for 12 hr and then vacuum desiccated for 24 hr to remove residual absorbed ethylene oxide gas. Surface cleaning and sterilization were conducted at standard temperature and pressure (i.e., 25°C and 1 bar).

2.3 | Sample characterization

A XANES study was used to determine the type of bonding that exists within the constituent surface elements of silicon nitride. The theory of XANES methodology can be found in Koningsberger and Roelof (1988). In this study, evaluations of the Si L- edge and Y M-edge were conducted at the National Synchrotron Light Source facility (Canadian Light Source, CLS, University of Saskatchewan, Saskatoon, Saskatchewan, Canada). Details of the beam energy for each studied element are given in previous publications (Ilyas et al., 2015, 2016; Varanasi et al., 2017) and in the Results section below. XANES analysis was used to determine the presence of Si-O, Si-N and Si-Si bonds and how the presence of Yttrium affects these coordination structures.

Three instruments were utilized in assessing the morphological surface features of the samples including atomic force microscopy (AFM, Park XE 70; Park Systems), a contact stylus surface profiler (Alpha Step IQ; KLA Tencor Corporation) and an optical profilometer (NPFLEX; Bruker). The stylus-based surface profiler analysed thin-step heights, surface micro-roughness and overall form error while providing sufficient vertical range for

Author Manuscript Author Manuscript Author Manuscript Author Manuscript

large topographical variations. The optical profilometer performed analyses over a larger surface area via non-contact mapping in three dimensions. It captured surface topography images and provided estimates of the different surface roughness parameters that were representative of the entire sample. The optical profilometer overcame some of the limitations imposed by small area analyses using AFM, and features that are smaller than the stylus tip diameter of the contact profiler.

The contact angles of deionized water and diiodomethane (>99% purity; Sigma-Aldrich) on the sample's surfaces were determined using sessile drop techniques. The images were captured using a high-speed camera (WATEC, high resolution, NAVITAR lens) synced to FTA32 software (First Ten Angstroms Inc). For each material, three samples were tested with 9 repetitive drops of DI water and diiodomethane at 25°C. Surface tensions, (γ^{LV}), including polar (γ^{d}) and dispersive (γ^{p}) components, for water and diiodomethane were 72.8, 21.8, and 51.0 mJ/m^2 and 50.8, 50.4, and 0.4 mJ/m^2, respectively (Amaral, Lopes, Santos, & Silva, 2002; Varanasi et al., 2017). The surface energy of each sample was calculated using the Owens–Wendt–Kaelble equation as described in prior work (Varanasi et al., 2017).

Each material was imaged for their respective surface morphology using an Ultra HR-SEM (Hitachi S-4800 II FE SEM; Hitachi). Prior to imaging, PEEK and Si_3N_4 samples were sputter-coated with conductive silver (CrC-100 sputter, Plasma Sciences Inc.). Images were acquired at a working distance 10 mm under 20 kV and at different magnifications. EDS mapping of sample surfaces after 7 days of immersion in α-MEM was observed with an energy-dispersive X-ray spectroscope (EDS) detector connected with a Hitachi S-3000N Variable Pressure SEM.

FT-IR and Raman spectroscopy were used to characterize mineral formation on the surface of all samples. These samples were immersed in α-MEM for 7 days. Thermo Nicolet 6700 FT-IR Spectrometer (Thermo Electron Corporation) equipped with a smart attenuated total reflectance (ATR) accessory was used to collect the FT-IR absorbance spectra over the range of 4,000–500 cm^{-1}, with an aperture 150, 128 scans and resolution of 4 cm^{-1}. Raman spectroscopy (DXR; Thermo Scientific Waltham) with a 780 nm excitation laser at 100 mW, 10× objective and a 50 μm slit was used for all samples except for PEEK, which needed a different set-up (1 mW, 10× objective and a 25 μm pinhole). The samples were photo-bleached for 4 min prior to spectra collection, and a 10-s exposure time was used. Thirty-two spectra per location were recorded between 400 and 2000 cm^{-1}.

X-ray diffraction was used to investigate HA formation on sample surfaces after 7 days of immersion in α-MEM. A Siemens D500 XRD system was used to collect scans using Cu Kα radiation (λ = 1.5418 Å) at room temperature. Data were recorded over the 2θ range of 20 – 80° with a 0.04° step size and a dwell time of 1.5 s.

2.4 | In vitro studies

Murine calvarial MC3T3-E1 osteoblast cells (American Type Cell Culture Inc.) were cultured in 75-sq. cm flasks (Corning Life Sciences Inc.) using α-MEM supplemented with 10% foetal bovine serum (FBS) and 1% penicillin/ streptomycin (pen-strep) until

Author Manuscript Author Manuscript Author Manuscript Author Manuscript

75%–90% confluence. These cells were used below passage 29 incubated at 37°C, 100% relative humidity and 5% CO_2 (according to the manufacturer's specifications). Ethylene oxide sterilized samples of each test material ($n = 3$) were washed twice with PBS, placed in 24-well plates and seeded with 10^5 MC3T3-E1 cells. All well plates used in this study were standard tissue culture plastic that was vacuum gas treated (Corning Life Sciences Inc.). The cell proliferation study was performed on both polished (2000 grit) and as-fired/as-machined samples (600 grit) to compare the cellular proliferation on both types of surface roughness. The in vitro studies for cellular differentiation and the gene expression were performed on as-machined samples for clinical relevance.

Cellular adhesion was studied by culturing cells on sample surfaces for 24 hr (Sista, Wen, Hodgson, & Pande, 2013). Since MC3T3-E1.4 cells have a doubling time at 36 hr, it is well accepted to investigate cell adhesion within 24 hr after cell seeding onto biomaterial surface such that colonies of cells can be easily viewed using various microscopy techniques. At the end of the experiment, the samples were washed in PBS twice to remove non-adherent cells. All samples were then removed from culture plates and transferred to fresh well plates. The samples were fixed using 2% glutaraldehyde (Sigma Inc.) for 1 hr. The samples were then sequentially alcohol dehydrated using an ethanol–water mixture using sequential concentrations of alcohol (i.e., 25%, 50%, 75% and 100%) to preserve the intact cellular structure on the sample surfaces. Cells were then imaged via SEM at various magnifications.

For cell proliferation studies, cells were cultured in a similar manner as adhesion study except for incubation periods of 1, 4 and 7 days. Samples were washed in PBS to remove non-adherent cells. Samples were removed from the incubation plates and transferred to fresh well plates with MTS reagent diluted with α-MEM (20% MTS reagent of total volume of MEM).

Samples were evaluated for cellular proliferation by an MTS Cell Proliferation Assay kit (MTS Aqueous One Assay; Promega Inc.). The MTS assay is a colorimetric method for determining the number of viable cells on sample surfaces. It determines the amount of formazan produced from the mitochondria of viable cells given the MTS reagent (tetrazolium reagent) (Coussens et al., 2004). The formazan dye transforms the colour of the culture media from a yellow (low cell density) to purple colour (high cell density). The colour of the solution was measured using a spectrophotometer (Spectromax Plus; Spectromax Inc.) at 540 nm. The measured optical density of the solution was converted to cell density using a calibration curve of cell density versus optical density.

RUNX2 was chosen for this study due to its vital role in stimulating osteoblast differentiation. It is stimulated when cells are exposed to ascorbic acid to induce osteoblast differentiation. Thus, to study the effect of these material surfaces on the expression of RUNX2, MC3T3-E1 cells were seeded on the different sample surfaces as described above. The cells were seeded and treated for 30 days with an ascorbic acid enriched medium (50 μg/ml ascorbic acid in α-MEM supplemented with 10% FBS and 1% penicillin/streptomycin) to induce cell differentiation. After 3 days of culture on the control surface (coverslip) and test samples, quantitative reverse transcriptase polymerase chain reaction (qRT-PCR) was performed as previously described (Varanasi, Saiz, et al., 2009). Briefly,

Author Manuscript Author Manuscript Author Manuscript Author Manuscript

cells were lysed, RNA extracted (RNeasy Mini kit; Qiagen) and converted to cDNA (Reverse Transcription System; Promega) using manufacturer guidelines. Samples were tested for runt-related transcription factor 2 (RUNX2, accession no. NM_009820.2) using glyceraldehyde 3-phosphate dehydrogenase (GAPDH, accession no. NM_008084.2) as internal housekeeping gene. Quantification of the relative gene expression was conducted using delta – delta CT (Δ – Δ-CT) method.

Scanning electron microscopy can provide insight into the ECM environment and the collagen fibres by the examination of tissue morphology. Also, EDX/EDS surface mapping can investigate the mineral deposition and detect Ca and P formation. Thus, SEM and EDX/EDS mapping were performed after 30 days of culture in differentiation media to investigate any collagen fibres, Ca or P deposition on the surface.

3 | RESULTS

Figure 1 represents the XANES measurements of silicon nitride's surface chemical coordination. The fluorescence signal (FY) data for Si L2, 3 edge (Figure 1a) represent the absorption energy of the p core–shell electrons for Si. Peaks a and b at 105.7 and 106.3 represent 2p spin-orbital splitting, which was described previously (Ilyas et al., 2015; Varanasi et al., 2017). These were observed in a shifted state in the as-fired and polished samples possibly indicating a change in the near-surface bonding of the Si atom. Transition of 2p to 3s/3d orbitals was observed at peak c near 108.1eV. Resonance peaks were observed in the post-edge data for Si_3N_4 samples but not seen in Si_3N_4 model compound data. This could indicate a shape change in the orbital (Bunker, 1984; Martin et al., 1995). Finally, the pre-edge peak at 104.5 ± 0.2 eV is the distinguishing peak between Si_3N_4 type bonding and SiO_2 type bonding. The pre-edge shoulder at this energy signifies the presence of Si-O and Si-N bonding. These results therefore confirm the formation of a silicon oxynitride surface with a random mixing of Si-O and Si-N bonding.

Given in Figure 1b is the total electron yield (TY) and fluorescence signal (FY) data for yttrium M-edge which represents the absorption of d electrons. Peaks a and b represent $3d_{3/2}$ and $3d_{1/2}$ orbital activity. They are 2eV apart and are expected to occur at 155.7 and 157.7 eV, respectively (Poole, 2017). Their resonance feature was observed at a′ and b′. The silicon nitride samples showed peaks a and b shifted to higher energies at 163.7 and 164.7 eV with just 1 eV difference between them. The peak at 156.5 is likely due to N 1-s peak resonance in the Y spectrum energy range. These shifts may have occurred due to a change in bonding or electrical coordination of elemental yttrium from its pure state as yttrium oxide to its combination with Si_3N_4. These results therefore indicate the shift in binding energy for electrons on the surface, which contributes to the overall surface energy.

Surface roughness parameters collected from the three different measurement techniques are shown in Table 1. It is important to note that these different measurement methods confirmed that polished silicon nitride samples had the lowest roughness parameters compared to the other samples. Results from both AFM (Figure 2) and optical profilometry showed that the PEEK 600 grit samples had the highest R_a and R_q values. While the stylus profilometer was effective in measuring general surface parameters, the AFM and

Author Manuscript Author Manuscript Author Manuscript Author Manuscript

optical profilometer provided detailed three-dimensional characterization of each sample's morphological features as shown in Figure 2. Thus, the average roughness according to the AFM and optical profilometer from highest to lowest was PEEK 600 grit > Si_3N_4 as-fired > PEEK 2000 grit > Ti6Al4V 600 grit > Ti6Al4V 2000 grit > Si_3N_4 polished. Both analyses confirmed the large difference in the surface topography between the as-fired and polished Si_3N_4, Ti6Al4V 600 grit and 2000 grit, and PEEK 600 and 2000 grit. As-fired Si_3N_4 showed a rougher and more granular surface whereas an even, non-granular surface was found for polished Si_3N_4.

Figure 3 provides the static water contact angles for each tested surface. Figure 4a shows the variation in contact angles on the sample surfaces with water and diiodomethane. Figure 4b presents the calculated surface energies (γ) broken into polar γ_p and dispersive γ_d components for each tested sample. It was observed that the magnitude of contact angle decreased as the surface roughness of the sample decreased. This was exemplified by comparing the contact angles for the as-fired silicon nitride ($\Theta = 65.13°$, $R_a = 309.27$ nm) and polished silicon nitride ($\Theta = 55.31°$, $R_a = 9.32$ nm). A similar result was observed for the Ti and PEEK samples. The effect of surface polishing reduced the prominence of peaks and valleys. This minimized entrapped air at the liquid–solid interface, thereby reducing the contact angle (Cassie, 1948). Figure 4c shows deionized water contact angles for all samples before and after immersion for 1, 4 and 7 days in α-MEM. The contact angles of all samples significantly decreased within the first day. Remarkably, the contact angles for the as-fired and polished Si_3N_4 samples decreased from 65.13° ± 2.9° and 58.50° ± 1.7° to 7.31° ± 4.1° and 7.05° ± 3.15°, respectively, during the first day and then gradually decreased to 0° and 2.89° after 7 days. Statistical analyses confirmed a significant decrease in the contact angle at 1, 4 and 7 days compared to day 0 of immersion in α-MEM (***$p < 0.001$).

SEM images of the bare sample surfaces' and the nanocrystalline HA formed on these surfaces with their representative EDS spectra are presented in Figure 5. Although these images provide clear evidence for the formation of HA on the surfaces of all samples, it was noted that its highest density and largest coverage occurred on the as-fired and polished Si_3N_4 samples. This was also confirmed from the measured HA-layer thickness as shown in the cross-section SEM images presented in Figure 6a-c. These images clearly delineated the HA layer on each sample's surface and allowed an estimate of its thickness using imaging software. The measured HA thickness exhibited the highest value of 54.8 ± 4.3 μm on the as-fired Si_3N_4 surface compared to 20.5 ± 3.5 μm, and 15.9 ± 2.3 μm for Ti6Al4V 600 and PEEK 600 grit samples, respectively, as presented in Figure 6d. Figure 6e shows the Ca/P ratio calculated from the EDS elemental analysis. The Ca/P ratio for HA formation on the as-fired and polished Si_3N_4 was 1.32 ± 0.03 and 1.42 ± 0.16, respectively. PEEK samples showed Ca/P ratio relatively similar to Si_3N_4, while HA formation on Ti surface had a lower Ca/P ratio, which indicates Ca deficiency in the surface formed HA layer.

Characterization of bare and in vitro immersed surfaces by Raman spectroscopy after 1, 4 and 7 days of incubation in α-MEM is given in Figure 7. Silicon nitride and Ti surfaces showed the formation of carbonate and phosphate peaks from the first day of immersion, while PEEK samples exhibited very little to no phosphate or carbonate species formation after day 7. Only, silicon nitride surfaces indicated the presence of amide, and

Author Manuscript Author Manuscript Author Manuscript Author Manuscript

hydroxyproline peaks from day 4 of immersion. The amide and phosphate peaks on Si_3N_4 surfaces increased in height as a function of in vitro immersion time, indicating their stability to remain bound to this bioactive surface.

FT-IR spectra of all samples after 7 days immersion in α-MEM confirmed the formation of HA as presented in Figure 8. These spectra indicated the presence of characteristic absorption bands for the vibrational modes of PO_4^{3-} that appeared around 1,019, 962 and 600 cm^{-1}. The broadband that appeared at 3,350–3550 cm^{-1} corresponded to strongly adsorbed and/or bound H_2O, as well as the weak bands of OH^- group that appeared at 3,572 and 595 cm^{-1}. Furthermore, the observed bands at 1,420–1465 and 875 cm^{-1} were attributed to the CO_2^{3-} group that substituted for the phosphate group in the apatite structure. These spectra are in agreement with other published data of the HA(Deng et al., 2015; Jia et al., 2009; Sanosh, Chu, Balakrishnan, Kim, & Cho, 2009; 2008, & Bressiani, 22008; Son et al., 2012). Of all the samples, only Si_3N_4 showed a weak broadband at 1600–1650 cm^{-1} corresponding to the N-H of amide I, which can explain the presence of amide peaks found in the Raman spectra.

To confirm the presence of HA-layer formation on the samples' surfaces, the structure of the formed layer compared to the bare samples surfaces was investigated by X-ray diffraction analysis. The patterns presented in Figure 9. XRD analysis supported the SEM, Raman and FT-IR results that indicated the formation of HA layer after in vitro testing. When the bare and the immersed surfaces of each sample were compared, two newly formed peaks appeared at 32° and 46° 2θ that related to (211) and (203) planes, respectively, of the nanocrystalline hydroxyapatite. The grain size of these HA crystals on each surface was estimated using the Debye–Sherrer relation (Kamal et al., 2015; Varanasi, Besmann, Hyde, Payzant, & Anderson, 2009; Varanasi et al., 2011). The estimated values confirmed that the grain size increases from 30.4 nm for the polished Si_3N_4 to reach 48.20 nm for the PEEK 2000 grit sample; this increase can explain the highest intensity of the (211) peak for PEEK 2000 grit sample. The lack of the "needle-like" structure of HA and more of a "flower-like" porous structure as seen in SEM images concur with the oriented polycrystalline grains seen in Figure 5. The (203) peak shift was likely due to a slight change of lattice parameters associated with compression or tension within the HA lattice.

AFM 3D images of the surfaces of the tested samples after 7 days of incubation in α-MEM are shown in Figure 2. After α-MEM immersion, each sample showed a "blister rough" surface compared to its bare surface (Figure 2). This blister-shape is indicative of the formation of nanocrystalline HA. Furthermore, the roughness parameters for all samples increased, which further suggests the deposition of HA. In particular, Figure 2d displays the topography of the polished Si_3N_4 sample after HA formation. This image clearly shows HA growth on the Si_3N_4 bare surface; the yellow arrows indicate the bare surface, and the black arrows refer to HA crystals formation. Table 1 presents the average roughness of the HA layer and indicates that the HA crystals on the as-fired Si_3N_4 had the highest roughness of any surface, also confirming the highest HA density on this surface.

Figure 10 shows the cellular adhesion on polished surfaces of silicon nitride, titanium (2000 grit) and PEEK (2000 grit). Figure 10a shows more cell spreading and a higher density of

Author Manuscript Author Manuscript Author Manuscript Author Manuscript

well-adherent cells on the surface of silicon nitride than PEEK (Figure 10c); however, it had comparable density and cell spreading to titanium (Figure 10b). The images indicate that polished silicon nitride and titanium are suitable surfaces for osteoblast adhesion and spreading.

Figure 10d,e shows cell proliferation on the different surfaces. Figure 10d compares as-fired silicon nitride, as-machined titanium and PEEK, and Figure 10e shows cellular proliferation on the polished surfaces for 1, 4 and 7 days. It was found that Si_3N_4 outperforms Ti and PEEK at a very early stage of seeding (1 day). Silicon nitride also facilitated significant proliferation of cells as compared to Ti and PEEK after 7 days of culture. This suggests that Si_3N_4 had a higher affinity for cell attachment at an early time-point, and it more readily facilitated cellular proliferation.

Figure 11a-c represents HR-SEM images on the surface of as-machined samples of Si_3N_4, Ti and PEEK, respectively, to study the mineral deposition and ECM formation after 30 days in the in vitro study. In Figure 11a, Si_3N_4 surface is completely covered with collagen fibres which bind together to form collagen bundles. Furthermore, mineral formation of calcium phosphate like deposition was found on the surface. SEM images also indicated that collagen fibres started to form collagen bundles (less dense than Si_3N_4) and sparse deposition of calcium phosphate like mineral deposition on Ti surface (Figure 11b). On the other hand, PEEK samples (Figure 11c) revealed the presence of collagen fibres (very sparse), but no collagen bundles. The EDX/EDS analysis identified the Ca and P deposition on the surface of Si_3N_4 samples indicated in Figure 11d. As-machined samples of Si_3N_4 and Ti show more than 2.5-fold difference for relative expression of osteoblastic differentiation gene marker RUNX2 at 3 days compared to the control (coverslip) and PEEK as indicated in Figure 11e (statistically different, $^{**}p < 0.01$).

Figure 12a-c represents the FT-IR spectra of the samples were seeded with MC3T3-E1 cells and cultured in differentiating media for 30 days. Both Si_3N_4 and Ti samples show the presence of collagen fibres compared to the PEEK sample that did not show any significant peaks for the ECM environment. The spectra indicate several vibrational bands related to the ECM component, such as ECM proteins (collagen) and P-O bonds of PO_4^{3-} ions on Si_3N_4 and Ti surfaces. The vibrational bands of amide I (peak a at 1637 cm^{-1}), amide II (peak b at 1532 cm^{-1}) and amide III (peak c at 1,228 cm^{-1}) indicate ECM proteins on both Si_3N_4 and Ti samples.

4 | DISCUSSION

The aim of this study was to characterize the surface properties of three clinically relevant biomaterials—Si_3N_4, Ti and PEEK—and subsequently assess their impact on the adhesion and proliferation of calvarial osteoprogenitor cells. Each material was tested at two different average surface roughnesses. In addition to roughness, surface energy and surface functional group formation were also examined (after in vitro immersion). In in vitro cell-free testing, silicon nitride surfaces formed the highest and most dense nanocrystalline HA layer. Silicon nitride (either as-fired or polished) outperformed titanium and PEEK in promoting

Author Manuscript Author Manuscript Author Manuscript Author Manuscript

osteoprogenitor cell growth. Cells were highly dense and well-adherent when in contact with the silicon nitride surfaces.

The increased cell growth on the Si_3N_4 samples was due in part to the difference in surface energy when compared with titanium and PEEK. Each material was evaluated for its surface energy by measuring the contact angle of polar and non-polar solvents. It is well-understood that the surface energy depends on the number of dangling or broken bonds (Gao, Sun, & Hu, 2014; Gao, Sun, Hu, & Liu, 2012; Hu, Gao, Sun, & Liu, 2012). By increasing the density of dangling bonds, the surface energy increases and the contact angle decreases. For the Si_3N_4 samples, the significant decrease in the contact angle can be attributed to the precipitation of calcium phosphates out of the α-MEM solution onto the sample surfaces that led to the formation of hydroxyapatite as confirmed by XRD and from the SEM images. The HA significantly enhanced the hydrophilic character of the surface which ultimately promoted cell proliferation and differentiation. The slightly increased cell growth on the polished Si_3N_4 compared to the rougher as-fired Si_3N_4 surface can be attributed to the nanostructured features on the rough surface that initially inhibit the cell attachment, but the highly reactive as-fired Si_3N_4 with its inherent surface properties lead to progressive transformation of cells towards enhanced osseointegration over time as reported by Ishikawa et al. (2017). For both PEEK and Ti6Al4V samples, their contact angles decreased significantly after the first day, but slightly increased again after 4 days. This later increase could be attributed to unstable precipitates on their surfaces. Conversely, the Si_3N_4 surfaces showed evidence of increased bonding density of other functional groups (amide I, amide II, hydroxyproline and CH_2) that were absent on the Ti and PEEK surfaces. The presence of these functional groups may explain why the Si_3N_4 samples' surface energies remained relatively low after 4 and 7 days as compared to Ti and PEEK.

The presence of surface functional groups on silicon nitride can also help explain the differences in cell adhesion and growth when compared to titanium and PEEK. On one hand, titanium and PEEK surfaces also showed formation of HA crystals. On the other hand, the Si_3N_4 surfaces appeared to form other functional groups that are present in collagenous extracellular matrix. The analysis by SEM of these surfaces showed a higher density of nanocrystalline HA as compared to titanium and PEEK (Figure 7). The nanocrystalline HA appeared to exhibit a porous, “flower-like” structure. Indeed, this structure was confirmed by XRD to be consistent with nanocrystalline HA. (Ramesh, Tan, Sopyan, Hamdi, & Teng, 2007; Sanosh et al., 2009; Turkez et al., 2014). Elemental analysis by EDS showed that the Ca/P ratio of the HA on the as-fired Si_3N_4 surface was 1.32. This ratio has been associated with octacalcium phosphate (~1.3 – 1.33) which is a precursor to hydroxyapatite (Brown & Brent, 2017). Interestingly, the polished Si_3N_4 surfaces induced nanocrystalline HA with a Ca/P ratio of 1.42, which is close to that of native HA ($Ca_{10}(PO_4)_6(OH)_2$: Ca/P = 1.66). For Ti or PEEK, nanocrystalline HA was confirmed with similar Ca/P ratio as that of as-fired Si_3N_4. Furthermore, the formation of HA structures on the Si_3N_4 surfaces was similar to that found in prior studies on amorphous silicon nitride (Varanasi et al., 2017). Combining the results from the SEM, EDS, XRD and Raman spectroscopy analyses, it is reasonable to attribute the enhanced osteoblast growth on the Si_3N_4 surfaces to the presence of these surface functional groups, relatively dense nanocrystalline HA formation and relatively high surface energy (i.e., low wetting angles).

Author Manuscript Author Manuscript Author Manuscript Author Manuscript

These unique properties of the bioactive Si_3N_4 surface lead to high expression of RUNX2 that was slightly higher compared to Ti. This contrasts with the control (coverslip) and PEEK samples which showed lower osteogenic effects. Furthermore, the Si_3N_4 surface outperformed both Ti and PEEK samples in mineral deposition and formation of dense collagenous ECM as confirmed from the SEM images and the FT-IR analysis. This can be attributed to the wettability, high surface energy and functional groups of the bioactive Si_3N_4 surface that lead to rapid cell differentiation and earlier ECM and mineral deposition. The poor ECM formation on the PEEK surfaces could be attributed to the low number of attached cells that result in low differentiation and poor ECM deposition. The observed biological differences are due to the nature of the considered surfaces, differences that can trigger the adsorption of different proteins and therefore different biological outcomes.

In a prior study using amorphous silicon oxide, silicon oxynitride and silicon nitride (Ilyas et al., 2015), the addition of nitrogen caused the surface silicon dioxide to become a mixture of both tetrahedral and trigonal coordination. The added N caused an increase in the carbonate/phosphate ratio and N-H bond density prior to testing in cell culture. It was also observed that a large density of collagenous ECM formed on this silicon nitride surface, and it was speculated that the increased N-H bonding could be integrated into the structure of the collagen via amine group bonding to the material's surface (Varanasi et al., 2017). In other investigations, it was found that N increased the expression of enzymes associated with collagen cross-linking such as superoxide dismutase and lysyl oxidase (Ilyas et al., 2016). The results from XANES analysis confirmed the presence of Si-O and Si-N bonding on the Si_3N_4 surface. Thus, it is reasonable to suggest that the surface of Si_3N_4 may have the presence of a silicon oxynitride layer. Future investigations will attempt to uncover this effect and provide evidence of the important role of nitrogen in bone regeneration and the impact of the Si-O-N elemental system on collagen formation.

It is known that nanometer size HA is the nuclei on which osteoblast cells build apatite crystals. However, these HA crystals are believed to form in the intracellular space (Nitiputri et al., 2016). Pezzotti et al. (2017) have observed similar findings in high-resolution transmission electron microscopy. Nevertheless, the spontaneous formation of Ca-P or HA on Si_3N_4 in the absence of cells has never been reported on the Si_3N_4 surfaces. However, our group has reported on this formation in previous work on silicon oxide, silicon oxynitride coatings (Ilyas et al., 2015, 2016; Varanasi et al., 2017). Kokubo et al. have extensively reported on the spontaneous formation of CaP on titanium and other implantable polymers (Kokubo, 1996). Thus, it was not surprising that precipitation of CaP crystals occurs when simulated body fluid (or cell culture medium) is used as an immersion environment. The formation of the amide peaks was also not surprising given prior results indicating that its formation occurs as a result of hydrogen bonding to the silicon–nitrogen–oxygen (Si-O-N) surface (Varanasi et al., 2017). Therefore, the formation of carbonate, phosphate, calcium, amide and hydroxyproline on these surfaces appears to be a characteristic solely observed on Si-N, Si-O and Si-O-N elemental constituent surfaces.

qRT-PCR gene expression results indicated that Ti surface highly expressed RUNX2 to a relatively similar level compared to Si_3N_4, this can be attributed to the presence of surface functional groups (PO_4^{3-} and CO_2^{3-}) and nanocrystalline HA on Si_3N_4 and Ti surfaces.

Author Manuscript Author Manuscript Author Manuscript Author Manuscript

Furthermore, the absence of these functional groups on the PEEK surface can explain its low expression of RUNX2. The RUNX2 expression results on Si_3N_4 are in agreement with what Ilyas et al previously reported on Si(ON)x surface (Ilyas et al., 2016); thus, it is possible to suggest that Si_3N_4 has a similar surface composition that leads to its bioactivity. On the other hand, the presence of amide I, amide II and hydroxyproline groups on Si_3N_4 surface can explain the complete ECM coverage on its surface compared to Ti and PEEK. Also, the limited coverage of ECM on Ti and PEEK surfaces as compared to Si_3N_4 can be explained as follows. For titanium, this could be due to the self-passivating nature of its surface with the formation of a TiO_2 layer. Although this layer promotes osteoblast attachment, it does not resorb (Martin et al., 1995). For PEEK surfaces, osteoprogenitor cells have demonstrated poor proficiency to differentiate into an osteoblast lineage and remain fibrogenic (Anselme, 2000; Lu, Lee, & Park, 1991; Olivares Navarrete et al., 2012; Pelletier et al., 2016). In this work, the key differences between these surfaces are their relatively low surface energies, a lack of surface functional groups that act as precursors for collagenous ECM formation, and relatively sparse deposition of HA crystals. Conversely, the surfaces of Si_3N_4 have been shown to exhibit Si-O and Si-N bonding as well as the formation of functional groups that promote collagenous biomineral deposition. This surface has been shown in a prior study to enhance osteogenic growth, collagen formation and osteogenic marker expression (Varanasi et al., 2017). It may be possible that the absence of amide and hydroxyproline causes delays in healing due to the relatively slow-growth of osteoblasts on Ti and PEEK surfaces. Future work will further analyse the effect of surface functionalization of silicon nitride on osteogenesis and possibly angiogenesis.

The difference in adsorption of functional groups on the surface of PEEK, Ti and Si3N4 was characterized by FT-IR and Raman analysis. The high negative charge on the silicon nitride surface as mentioned in previous literature leads to the hypersaturation of calcium ions in vitro leading to the increased precipitation of hydroxyapatite on these surfaces. Also, the relatively low surface energy of PEEK versus Ti or Si3N4 manifests as delayed or mitigated hydroxyproline and amide groups needed for collagen formation. This can lead to delays in the adhesion of actin, focal adhesion kinase, integrins and fibronectin proteins that help to establish the ECM on the biomaterial surface. This delay helps to explain the reason for PEEK's poor performance in this study and others in which surface modification with HA is needed to improve biomineral synthesis in vitro and in vivo. On the other hand, Ti and Si3N4 exhibit marked presence of collagen and hydroxyproline on their respective surfaces, thereby indicating the their relatively high surface energy is amenable to increased collagen formation and likely an improved outcome for biomineral formation in vitro and in vivo.

The ability of a material to induce rapid cell growth is an indicator of its potential to hasten healing and improve the potential for osteointegration by facilitating cellular attachment and growth. In the application of these materials in bone fixation, each has shown varying effects on promoting bone growth. Based on the results of this study, the various surfaces of silicon nitride exhibited high surface energy (i.e., low wetting angles) which facilitated the rapid growth of cells. These are promising signs that silicon nitride could be a viable alternative relative to titanium and PEEK for use in craniofacial bone defect reconstruction and where osseous integration is desired. This is coupled with the fact that prior work also showed the positive impact of silicon nitride on osteogenesis and

Author Manuscript Author Manuscript Author Manuscript Author Manuscript

bone regeneration. Further investigation in potentially integrating silicon nitride on bone regeneration and reconstruction in complex craniofacial defects, fractures and as implants is underway. It is clear from the current work coupled with prior studies that silicon nitride plays a significant scientific role in collagen formation, biomineral deposition and enhanced osteoblast proliferation.

5 | CONCLUSION

In this study, a comparative analysis of the effect of surface properties of various fixative bone implant materials was conducted. Silicon nitride, titanium and polyether ether ketone were compared. It was found that cells were well-adherent, relatively high in density, and grew at a relatively faster rate on silicon nitride surfaces as compared to titanium and PEEK. Silicon nitride's surface energy and surface functional group formation were determined to contribute to this result. Silicon nitride surfaces exhibited lower contact angles (i.e., higher surface energy) and were deemed more hydrophilic as compared to titanium or PEEK. Their improved wettability facilitated increased potential for cell migration and growth. This favourable wetting was coupled with the rapid formation of nanocrystalline HA along with amide functional group precursors important for collagen formation. Titanium and PEEK did not exhibit this coupled effect; therefore, it is concluded that the higher surface energy, formation of collagen precursor functional groups and biomineral on the surface of silicon nitride enabled well-adherent, rapid growing cells and later enhanced differentiation as compared to titanium and PEEK. In conclusion, Si_3N_4 outperformed conventional craniofacial implant materials due to its ability to enhance the osteoprogenitor cell adhesion, growth and differentiation via higher surface energy and the presence of amide and nanocrystalline HA functional groups.

ACKNOWLEDGEMENTS

The authors would like to thank Dr. Simon Young from the University of Texas Health Science Center at Houston, Brotto lab members, and Varanasi research group at UTA. Also, we would like to acknowledge the Nano Technology Research Center (NRC) and the Characterization Center for Materials and Biology (CCMB) at UTA. Deep thanks to the college of Nursing and Health Innovation and the provost office at the University of Texas at Arlington for supporting and funding this study under the grant of Science and Technology Acquisition and Retention (STARs Program, P.I. Venu Varanasi).

REFERENCES

Abu Bakar MS, Cheng MHW, Tang SM, Yu SC, Liao K, Tan CT … Cheang P (2003). Tensile properties, tension-tension fatigue and biological response of polyetheretherketone-hydroxyapatite composites for load-bearing orthopedic implants. Biomaterials, 24(13), 2245–2250. [PubMed: 12699660]

Amaral M, Lopes MA, Santos JD, & Silva RF (2002). Wettability and surface charge of Si3N4-bioglass composites in contact with simulated physiological liquids. Biomaterials, 23(20), 4123–4129. [PubMed: 12182314]

Anselme K (2000). Osteoblast adhesion on biomaterials. Biomaterials, 21(7), 667–681. [PubMed: 10711964]

Bal BS, & Rahaman MN (2012). Orthopedic applications of silicon nitride ceramics. Acta Biomaterialia, 8(8), 2889–2898. [PubMed: 22542731]

Author Manuscript Author Manuscript Author Manuscript Author Manuscript

Bloyer DR, Gomez-Vega JM, Saiz E, McNaney JM, Cannon RM, & Tomsia AP (1999). Fabrication and characterization of a bioactive glass coating on titanium implant alloys. Acta Materialia, 47(15), 4221–4224.

Bock R, Jones E, Ray D, Sonny Bal B, … Pezzotti G, & McEntire B (2017). Bacteriostatic behavior of surface modulated silicon nitride in comparison to polyetheretherketone and titanium. Journal of Biomedical Materials Research. Part A, 105(5), 1521–1534. [PubMed: 28000413]

Bock RM, Marin E, Rondinella A, Boschetto F, Adachi T, McEntire BJ, … Pezzotti G (2018). Development of a SiYAlON glaze for improved osteoconductivity of implantable medical devices. Journal of Biomedical Materials Research Part B: Applied Biomaterials, 106(3), 1084–1096. [PubMed: 28503805]

Bock RM, McEntire BJ, Bal BS, Rahaman MN, Boffelli M, & Pezzotti G (2015). Surface modulation of silicon nitride ceramics for orthopaedic applications. Acta Biomaterialia, 26, 318–330. [PubMed: 26302831]

Braem A, Mattheys T, Neirinck B, Čeh M, Novak S, Schrooten J, … Vleugels J (2012). Bioactive glass–ceramic coated titanium implants prepared by electrophoretic deposition. Materials Science and Engineering: C, 32(8), 2267–2273.

Brown PW, & Brent C (2017). Hydroxyapatite and Related Materials. Boca Raton, FL: CRC Press: Technology & Engineering, 35 of 368 pages.

Bunker G (1984). Interpreting XANES.

Cassie ABD (1948). Contact angles. Discussions of the Faraday Society, 3, 11–16.

Chou AHK, LeGeros R, Chen Z, & Li Y (2007). Antibacterial effect of zinc phosphate mineralized guided bone regeneration membranes. Implant Dentistry, 16(1), 89–100. [PubMed: 17356375]

Chou BY, & Chang E (1999). Microstructural characterization of plasma-sprayed hydroxyapatite-10 wt% ZrO_2 composite coating on titanium. Biomaterials, 20(19), 1823–1832. [PubMed: 10509193]

Coussens N, Brimacombe K, Grossman A, Arkin M, Auld D, Austin C, … Sittampalam GS (2004). Cell viability assays assay guidance manual.

Dabrowski B, Swieszkowski W, Godlinski D, & Kurzydlowski K (2010). Highly porous titanium scaffolds for orthopaedic applications. Journal of Biomedical Materials Research. Part B, Applied Biomaterials, 95(1), 53–61. [PubMed: 20690174]

Deng Y, Liu X,Xu A, Wang L, Luo Z, Zheng Y, … Wei S (2015). Effect of surface roughness on osteogenesis in vitro and osseointegration in vivo of carbon fiber-reinforced polyetheretherketone–nanohydroxyapatite composite. International Journal of Nanomedicine, 10, 1425–1447. [PubMed: 25733834]

Dorozhkin S (2015). Calcium orthophosphate-containing biocomposites and hybrid biomaterials for biomedical applications. Journal of Functional Biomaterials, 6(3), 708–832. [PubMed: 26262645]

e Silva CCG, da Silva Rigo EC, Marchi J, de Almeida Bressiani AH, & Bressiani JC (2008). Hydroxyapatite coating on silicon nitride surfaces using the biomimetic method. Materials Research, 11, 47–50.

Filiaggi MJ, Pilliar RM, & Coombs NA (1993). Post-plasma-spraying heat treatment of the HA coating/Ti-6A1-4V implant system. Journal of Biomedical Materials Research, 27(2), 191–198. [PubMed: 8436575]

Gao Z-Y, Sun W, & Hu Y-H (2014). Mineral cleavage nature and surface energy: Anisotropic surface broken bonds consideration. Transactions of Nonferrous Metals Society of China, 24(9), 2930–2937.

Gao Z-Y, Sun W, Hu Y-H, & Liu X-W (2012). Anisotropic surface broken bond properties and wettability of calcite and fluorite crystals. Transactions of Nonferrous Metals Society of China, 22(5), 1203–1208.

Gomez Vega JM, Saiz E, Tomsia AP, Marshall GW, & Marshall SJ (2000). Bioactive glass coatings with hydroxyapatite and bioglass particles on Ti-based implants. 1. Processing. Biomaterials, 21(2), 105–111. [PubMed: 10632392]

Gorth DJ, Puckett S, Ercan B, Webster TJ, Rahaman M, & Bal BS (2012). Decreased bacteria activity on Si(3)N(4) surfaces compared with PEEK or titanium. International Journal of Nanomedicine, 7, 4829–4840. [PubMed: 22973102]

Author Manuscript Author Manuscript Author Manuscript Author Manuscript

Hayashi K, Matsuguchi N, Uenoyama K, Kanemaru T, & Sugioka Y (1989). Evaluation of metal implants coated with several types of ceramics as biomaterials. Journal of Biomedical Materials Research, 23(11), 1247–1259. [PubMed: 2606919]

Hu Y, Gao Z, Sun W, & Liu X (2012). Anisotropic surface energies and adsorption behaviors of scheelite crystal. Colloids and Surfaces A: Physicochemical and Engineering Aspects, 415, 439–448.

Ilyas A, Lavrik N, Kim HKW, Aswath P, & Varanasi V (2015). Enhanced interfacial adhesion and osteogenesis for rapid "bone-like" biomineralization by PECVD-based silicon oxynitride overlays. ACS Applied Materials & Interfaces, 7(28), 15368–15379. [PubMed: 26095187]

Ilyas A, Odatsu T, Shah A, Monte F, Kim HKW, Kramer P, … Varanasi V (2016). Amorphous silica: A new antioxidant role for rapid critical-sized bone defect healing. Advanced Healthcare Materials, 5(17), 2199–2213. [PubMed: 27385056]

Ishikawa M, de Mesy Bentley KL, McEntire B, Bal BS, Schwarz E, & Xie C (2017). Surface topography of silicon nitride affects anti-microbial and osseointegrative properties of tibial implants in a murine model. Journal of Biomedical Materials Research. Part A, 105(12), 3413–3421. [PubMed: 28865177]

Itoh S, Kikuchi M, Takakuda K, Nagaoka K, Koyama Y, Tanaka J, & Shinomiya K (2002). Implantation study of a novel hydroxyapatite/collagen (HAp/col) composite into weight-bearing sites of dogs. Journal of Biomedical Materials Research, 63(5), 507–515. [PubMed: 12209894]

Iwai-Yoshida M, Shibata Y, Wurihan, Suzuki D, Fujisawa N, Tanimoto Y, … Miyazaki T (2012). Antioxidant and osteogenic properties of anodically oxidized titanium. Journal of the Mechanical Behavior of Biomedical Materials, 13, 230–236. [PubMed: 22944262]

Jia X, Zhou Y, Tan L, Xie Q, Tang H, Ma M, & Yao S (2009). Hydroxyapitite-multiwalled carbon nanotubes nanocomposite for adhesion and electrochemical study of human osteoblast-like cells (MG-63). Electrochimica Acta, 54(13), 3611–3617.

Jokstad A (2004). Common complications with implants and implant prostheses. Evidence-Based Dentistry, 5(3), 70–71. [PubMed: 15448647]

Jones JD, Saigusa M, Van Sickels JE, Tiner BD, & Gardner WA (1997). Clinical evaluation of hydroxyapatite-coated titanium plasma-sprayed and titanium plasma-sprayed cylinder dental implants: A preliminary report. Oral Surgery, Oral Medicine, Oral Pathology, Oral Radiology and Endodontology, 84(2), 137–141.

Kamal RA, Wahsh MMS, Othman AGM, Girgis E, Mabrouk MR, & Fatma AM (2015). Effect of Mn 2+ doping and SiO 2 coating on magneto-optical properties of CoFe 2 O 4 nano-particles. Smart Materials and Structures, 24(11), 115002.

Klein CP, Patka P, van der Lubbe HB, Wolke JG, & de Groot K (1991). Plasma-sprayed coatings of tetracalciumphosphate, hydroxyl-apatite, and alpha-TCP on titanium alloy: An interface study. Journal of Biomedical Materials Research, 25(1), 53–65. [PubMed: 1850430]

Kokubo T (1996). Formation of biologically active bone-like apatite on metals and polymers by a biomimetic process. Thermochimica Acta, 280–281, 479–490.

Koningsberger DC, & Prins R (1988). X-ray absorption: principles, applications, techniques of EXAFS, SEXAFS, and XANES. New York, NY: John Wiley and Sons, None: p Medium: X; Size: Pages: 684.

Kulkarni Aranya A, Pushalkar S, Zhao M, LeGeros R, Zhang Y, & Saxena D (2017). Antibacterial and bioactive coatings on titanium implant surfaces. Journal of Biomedical Materials Research. Part A, 105(8), 2218–2227. [PubMed: 28380669]

Kurtz S, & Devine J (2007). PEEK biomaterials in trauma, orthopedic, and spinal implants. Biomaterials, 28(32), 4845–4869. [PubMed: 17686513]

Laure B, Besnier J-M, Bergemer Fouquet A-M, Marquet-Van Der Mee N, Damie F, Quentin R, … Rosset P (2008). Effect of hydroxyapatite coating and polymethylmethacrylate on stainless steel implant-site infection with *Staphylococcus epidermidis* in a sheep model. Journal of Biomedical Materials Research. Part A, 84(1), 92–98. [PubMed: 17600319]

Lazarinis S, Mäkelä KT, Eskelinen A, Havelin L, Hallan G, Overgaard S, … Hailer NP (2017). Does hydroxyapatite coating of uncemented cups improve long-term survival? An analysis of 28,605

Author Manuscript Author Manuscript Author Manuscript Author Manuscript

primary total hip arthroplasty procedures from the Nordic Arthroplasty Register Association (NARA). Osteoarthritis and Cartilage, 25(12), 1980–1987. [PubMed: 28802851]

Lee H-B, Hsu H-C, Wu S-C, Hsu S-K, Wang P-H, & Ho W-F (2016). Microstructure and characteristics of calcium phosphate layers on bioactive oxide surfaces of air-sintered titanium foams after immersion in simulated body fluid. Materials, 9(12), 956.

Liu HY, Wang XJ, Wang LP, Lei FY, Wang XF, & Ai HJ (2008). Effect of fluoride-ion implantation on the biocompatibility of titanium for dental applications. Applied Surface Science, 254(20), 6305–6312.

Lu DR, Lee SJ, & Park K (1991). Calculation of solvation interaction energies for protein adsorption on polymer surfaces. Journal of Biomaterials Science. Polymer Edition, 3(2), 127–147. [PubMed: 1768635]

Lusquiños F, del Val J, Arias-González F, Comesaña R, Quintero F, … Riveiro A, Pou J (2014). Bioceramic 3D implants produced by laser assisted additive manufacturing. Physics Procedia, 56(Supplement C), 309–316.

MacInnes SJ, Gordon A, & Wilkinson JM (2012). Risk factors for aseptic loosening following total hip arthroplasty. In Fokter S (Ed.), Recent advances in arthroplasty (pp. 275–294). London, UK: InTech.

Martin JY, Schwartz Z, Hummert TW, Schraub DM, Simpson J, Lankford J, … Boyan BD (1995). Effect of titanium surface roughness on proliferation, differentiation, and protein synthesis of human osteoblast-like cells (MG63). Journal of Biomedical Materials Research, 29(3), 389–401. [PubMed: 7542245]

Mazzocchi M, & Bellosi A (2008). On the possibility of silicon nitride as a ceramic for structural orthopaedic implants. Part I: Processing, microstructure, mechanical properties, cytotoxicity. Journal of Materials Science: Materials in Medicine, 19(8), 2881–2887. [PubMed: 18347952]

McEntire BJ, Lakshminarayanan R, Thirugnanasambandam P, Sampson JS, Bock R, & Brien DO (2016). Processing and characterization of silicon nitride bioceramics. Bioceramics Development and Applications, 6(93), 1–10.

National Center for Health Statistics (2006). National Ambulatory Medical Care Survey 1998-2006. 2006 ed.; U.S. Department of Health and Human Services, C. f. D. C. a. P., Ed. National Center for Health Statistics, 2006.

Nitiputri K, Ramasse Q, Autefage H, McGilvery C, Boonrungsiman S, Evans N, … Porter A (2016). Nanoanalytical electron microscopy reveals a sequential mineralization process involving carbonate-containing amorphous precursors. ACS Nano, 10(7), 6826–6835. [PubMed: 27383526]

Oku T, Suganuma K, Wallenberg LR, Tomsia AP, Gomez Vega JM, & Saiz E (2001). Structural characterization of the metal/glass interface in bioactive glass coatings on Ti-6Al-4V. Journal of Materials Science: Materials in Medicine, 12(5), 413–417. [PubMed: 15348280]

Olivares Navarrete R, Gittens R, Schneider J, Hyzy S, Haithcock D, Ullrich P, … Boyan B (2012). Osteoblasts exhibit a more differentiated phenotype and increased bone morphogenetic protein production on titanium alloy substrates than on poly-ether-ether-ketone. Spine Journal, 12(3), 265–272.

Pelletier M, Cordaro N, Punjabi V, Waites M, Lau A, & Walsh W (2016). PEEK versus Ti interbody fusion devices: resultant fusion, bone apposition, initial and 26-week biomechanics. Clinical Spine Surgery, 29(4), E208–E214. [PubMed: 22801456]

Petrovic L, Pohle D, Münstedt H, Rechtenwald T, Schlegel KA, & Rupprecht S (2006). Effect of betaTCP filled polyetheretherketone on osteoblast cell proliferation in vitro. Journal of Biomedical Science, 13(1), 41–46. [PubMed: 16228286]

Pezzotti G, Bock RM, Adachi T, Rondinella A, Boschetto F, Zhu W, … Mazda O (2017). Silicon nitride surface chemistry: A potent regulator of mesenchymal progenitor cell activity in bone formation. Applied Materials Today, 9(Supplement C), 82–95.

Pezzotti G, McEntire BJ, Bock R, Boffelli M, Zhu W, Vitale E, … Bal BS (2016). Silicon nitride: A synthetic mineral for vertebrate biology. Scientific Reports, 6, 31717. [PubMed: 27539146]

Pezzotti G, McEntire BJ, Bock R, Zhu W, Boschetto F, Rondinella A, … Bal BS (2016). In situ spectroscopic screening of osteosarcoma living cells on stoichiometry-modulated silicon nitride

Author Manuscript Author Manuscript Author Manuscript Author Manuscript

bioceramic surfaces. ACS Biomaterials Science & Engineering, 2(7), 1121–1134. [PubMed: 33465870]

Poole DM (2017). X-ray absorption edges, characteristic X-ray lines and fluorescence yields.

Ramesh S, Tan CY, Sopyan I, Hamdi M, & Teng WD (2007). Consolidation of nanocrystalline hydroxyapatite powder. Science and Technology of Advanced Materials, 8(1–2), 124–130.

Rao P, Pelletier M, Walsh W, & Mobbs R (2014). Spine interbody implants: Material selection and modification, functionalization and bioactivation of surfaces to improve osseointegration. Orthopaedic Surgery, 6(2), 81–89. [PubMed: 24890288]

Saffarian Tousi N, Velten M, Bishop T, Leong K, Barkhordar N, Marshall G, … Varanasi V (2013). Combinatorial effect of Si4+,Ca2+, and Mg2+ released from bioactive glasses on osteoblast osteocalcin expression and biomineralization. Materials Science & Engineering. C, Biomimetic Materials, Sensors and Systems, 33(5), 2757–2765.

Sanosh KP, Chu M-C, Balakrishnan A, Kim TN, & Cho S-J (2009). Utilization of biowaste eggshells to synthesize nanocrystalline hydroxyapatite powders. Materials Letters, 63(24), 2100–2102.

Sista S, Wen C, Hodgson PD, & Pande G (2013). Expression of cell adhesion and differentiation related genes in MC3T3 osteoblasts plated on titanium alloys: Role of surface properties. Materials Science & Engineering. C, Materials for Biological Applications, 33(3), 1573–1582. [PubMed: 23827610]

Son KD, Yang DJ, Kim MS, Kang I-K, Kim SY, & Kim Y-J (2012). Effect of alginate as polymer matrix on the characteristics of hydroxyapatite nanoparticles. Materials Chemistry and Physics, 132(2), 1041–1047.

Song W-H, Ryu H, & Hong S-H (2009). Antibacterial properties of Ag (or Pt)-containing calcium phosphate coatings formed by microarc oxidation. Journal of Biomedical Materials Research. Part A, 88(1), 246–254. [PubMed: 18286618]

Steinberg EL, Rath E, Shlaifer A, Chechik O, Maman E, & Salai M (2013). Carbon fiber reinforced PEEK Optima–a composite material biomechanical properties and wear/debris characteristics of CF-PEEK composites for orthopedic trauma implants. Journal of the Mechanical Behavior of Biomedical Materials, 17, 221–228. [PubMed: 23127632]

Teraoka K, Nonami T, Doi Y, Taoda H, Naganuma K, Yokogawa Y, & Kameyama T (2000). Hydroxyapatite implantation on the surface of pure titanium for orthopedic implants. Materials Science and Engineering: C, 13(1), 105–107.

Transparency Market Research (2016). Bone grafts and substitutes market by product (allografts, bone grafts substitutes, and cell-based matrices), by application (spinal fusion, long bone, foot & ankle, craniomaxillofacial, joint reconstruction, and dental bone grafting). In Transparency Market Research, 2016, Global Opportunity Analysis and Industry Forecast: www.alliedmarketresearch.com, 2015–2023; Vol. 2015–2023.

Turk C, Halici M, Guney A, Akgun H, Sahin V, & Muhtaroglu S (2004). Promotion of fracture healing by vitamin E in rats. Journal of International Medical Research, 32(5), 507–512. [PubMed: 15458283]

Turkez H, Yousef M,Sönmez E, Togar BA, Bakan F, Sozio P, & DiStefano A (2014). Evaluation of cytotoxic, oxidative stress and genotoxic responses of hydroxyapatite nanoparticles on human blood cells. Journal of Applied Toxicology, 34(4), 373–379. [PubMed: 24474238]

van Oirschot BA, Alghamdi HS, Närhi TO, Anil S, Al Farraj Aldosari A, van denBeucken JJ, & Jansen J (2014). In vivo evaluation of bioactive glass-based coatings on dental implants in a dog implantation model. Clinical Oral Implants Research, 25(1), 21–28. [PubMed: 23078340]

Varanasi VG, Besmann TM, Hyde RL, Payzant EA, & Anderson TJ (2009). MOCVD of YSZ coatings using β-diketonate precursors. Journal of Alloys and Compounds, 470(1), 354–359.

Varanasi VG, Besmann TM, Payzant EA, Pint BA, Lothian JL, & Anderson TJ (2011). High-growth rate YSZ thermal barrier coatings deposited by MOCVD demonstrate high thermal cycling lifetime. Materials Science and Engineering: A, 528(3), 978–985.

Varanasi V, Ilyas A, Velten M, Shah A, Lanford W, & Aswath P (2017). Role of hydrogen and nitrogen on the surface chemical structure of bioactive amorphous silicon oxynitride films. Journal of Physical Chemistry. B, 121(38), 8991–9005. [PubMed: 28825836]

Author Manuscript Author Manuscript Author Manuscript Author Manuscript

Varanasi VG, Saiz E, Loomer PM, Ancheta B, Uritani N, Ho SP, … Marshall GW (2009). Enhanced osteocalcin expression by osteoblast-like cells (MC3T3-E1) exposed to bioactive coating glass (SiO2-CaO-P2O5-MgO-K2O-Na2O system) ions. Acta Biomaterialia, 5(9), 3536–3547. [PubMed: 19497391]

Webster TJ, Patel AA, Rahaman MN, & Sonny Bal B (2012). Anti-infective and osteointegration properties of silicon nitride, poly(ether ether ketone), and titanium implants. Acta Biomaterialia, 8(12), 4447–4454. [PubMed: 22863905]

Zanotti B, Zingaretti N, Verlicchi A, Robiony M, Alfieri A, & Parodi P (2016). Cranioplasty: Review of materials. Journal of Craniofacial Surgery, 27(8), 2061–2072. [PubMed: 28005754]

Zhao L, Chu P, Zhang Y, & Wu Z (2009). Antibacterial coatings on titanium implants. Journal of Biomedical Materials Research. Part B, Applied Biomaterials, 91(1), 470–480. [PubMed: 19637369]

Author Manuscript Author Manuscript Author Manuscript Author Manuscript

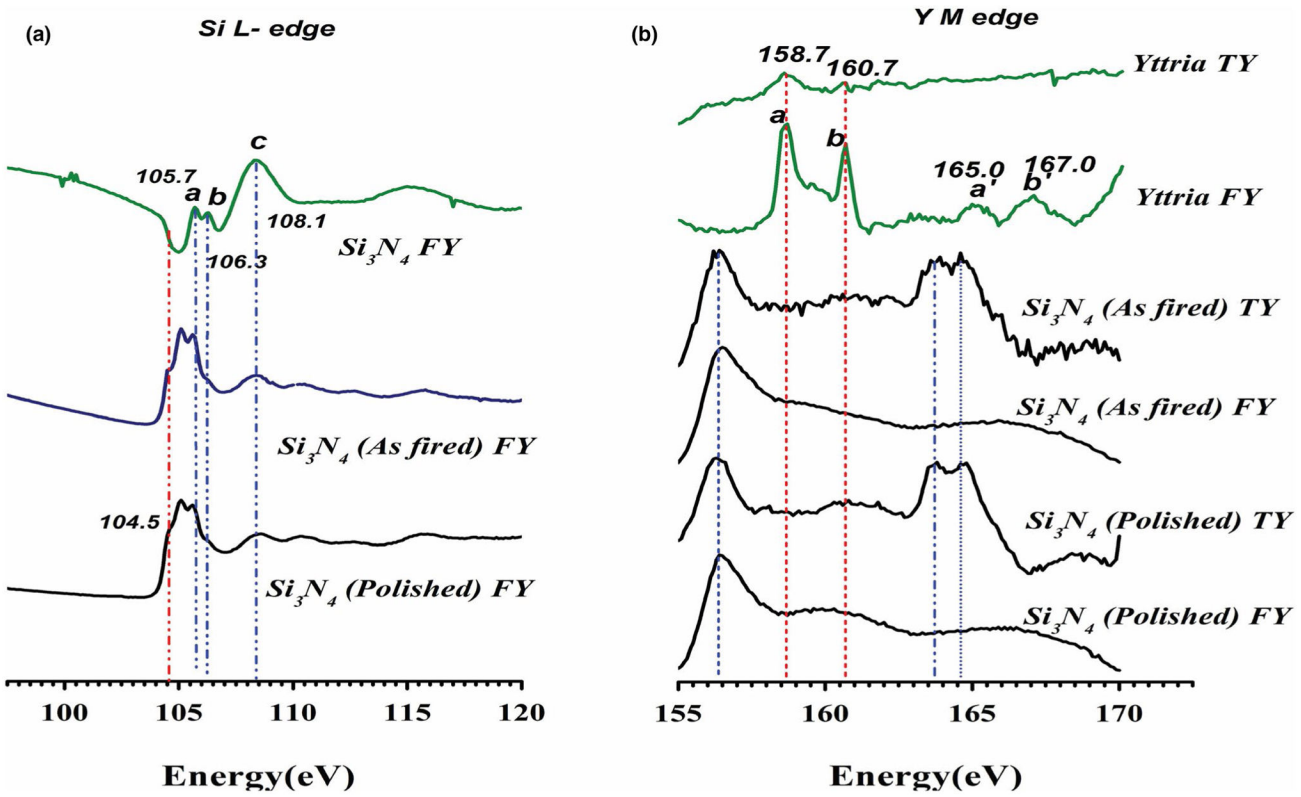

FIGURE 1.

XANES analysis of as-fired and polished Si_3N_4 showing (a) Si-$L_{2,3}$ edge and (b) Yttrium M-edge

Author Manuscript Author Manuscript Author Manuscript Author Manuscript

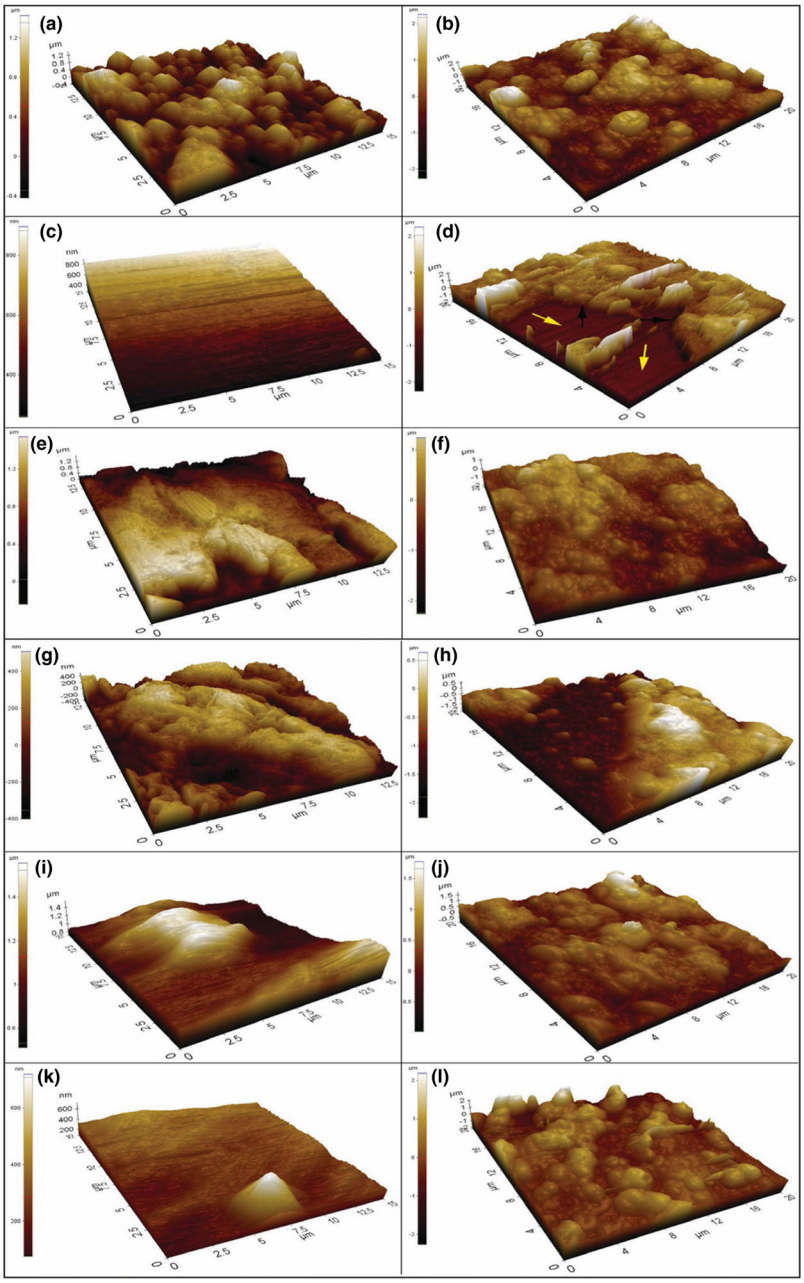

FIGURE 2.

3D-AFM images showing the surface topography before and after HA formation, respectively, (a, b) as-fired Si_3N_4, (c, d) polished Si_3N_4, (e, f) PEEK, 600 grit, (g, h) PEEK, 2000 grit, (i, j) Ti6Al4V 600 grit and (k, l) Ti6Al4V 2000 grit with colour indicator for determination of height

Author Manuscript Author Manuscript Author Manuscript Author Manuscript

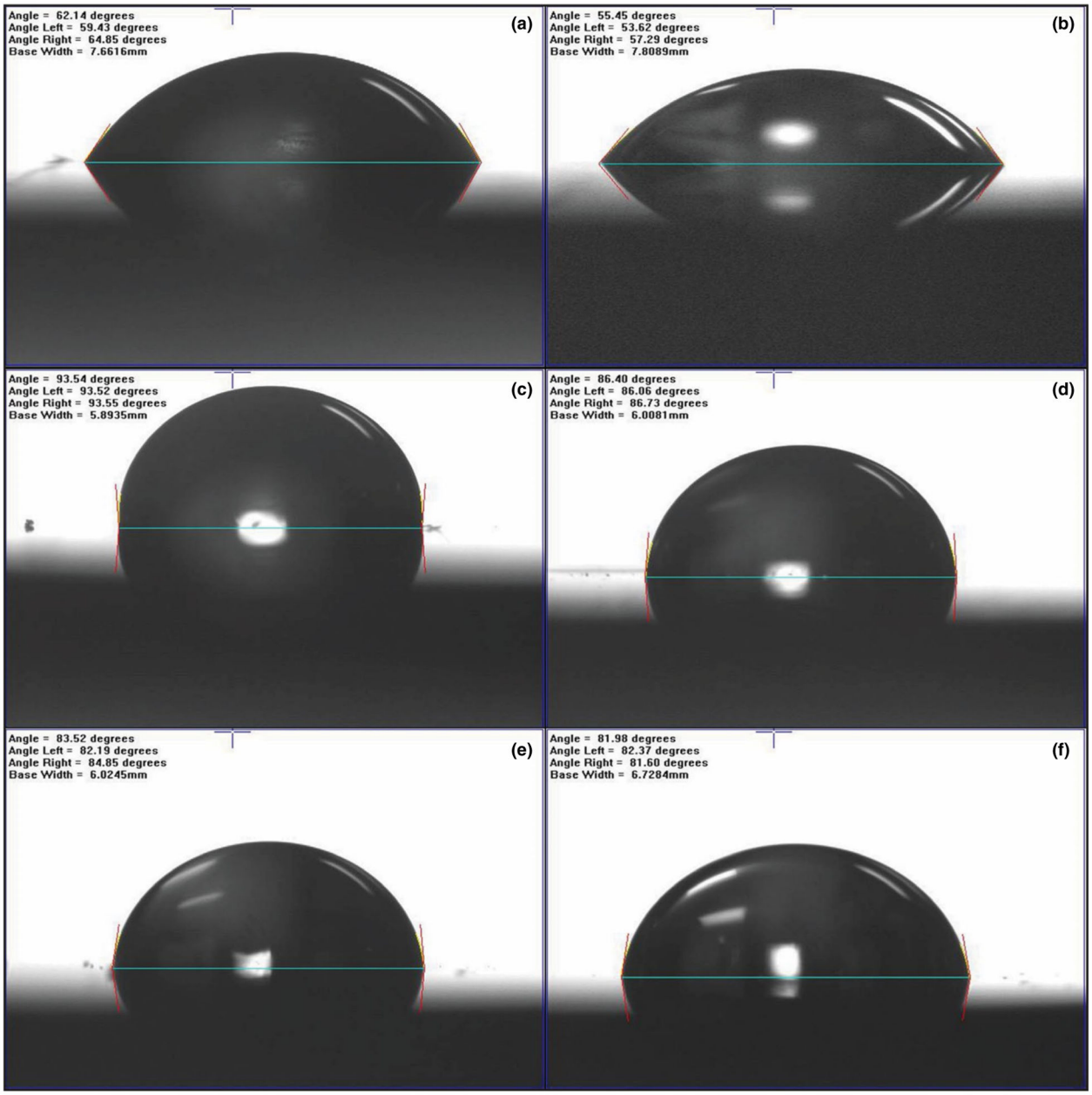

FIGURE 3.

Static contact angle images of water on the surface of (a) as-fired Si_3N_4, (b) polished Si_3N_4 (c) PEEK, 600 grit, (d) PEEK, 2000 grit, (e) Ti6Al4V 600 grit and (f) Ti6Al4V 2000 grit. The Si_3N_4 samples show an acute angle suggestive of hydrophilic surfaces as compared to PEEK and titanium

Author Manuscript Author Manuscript Author Manuscript Author Manuscript

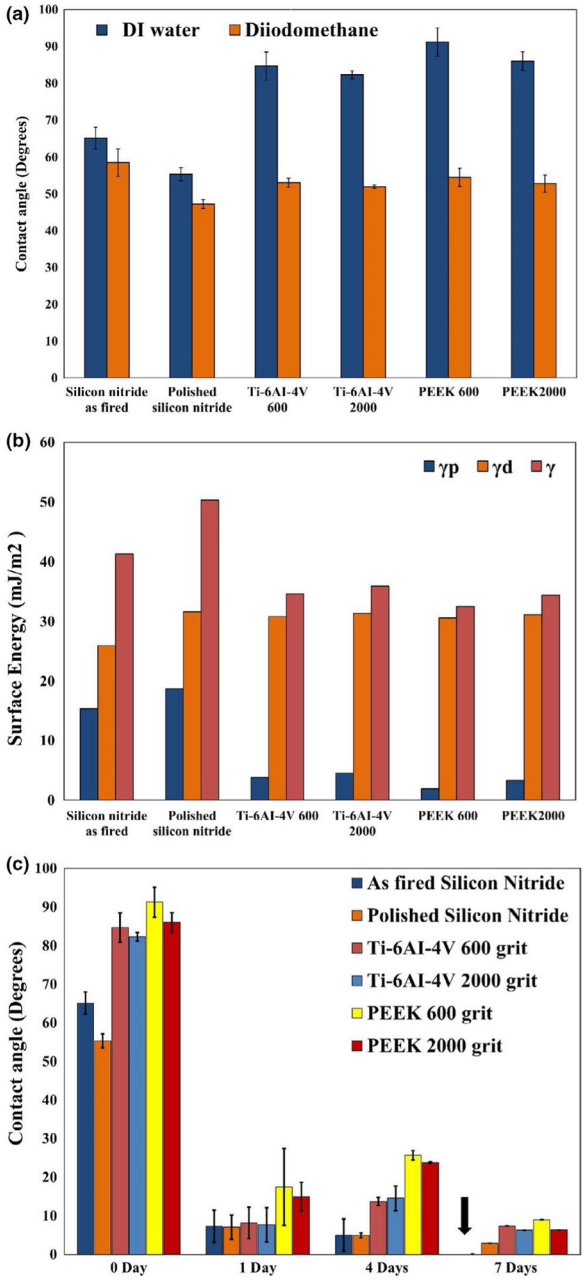

FIGURE 4.

Shows variation in contact angle on samples surface with water and DIM with error bars showing standard deviation (a), the calculated surface energy (γ) for all samples, broken into polar γ^{p} and dispersive γ^{d} components (b), and (c) indicates the variation in contact angle of DI water on the sample surface before and after immersion for 1, 4 and 7 days in α-MEM showing increasing in the hydrophilicity of the sample surface, and error bars showing the standard deviation

Author Manuscript Author Manuscript Author Manuscript Author Manuscript

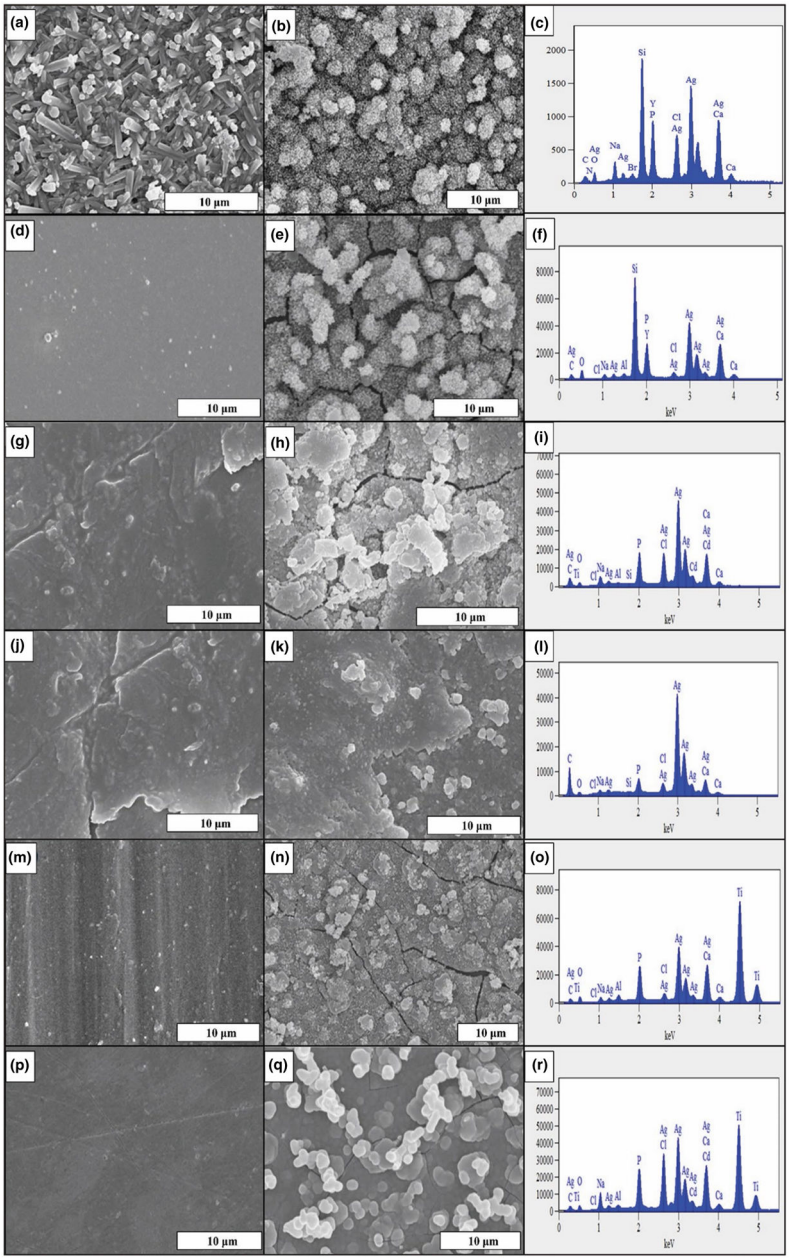

FIGURE 5.

HR-SEM images before and after 7 days in α-MEM of (a, b) as-fired Si_3N_4, (d, e) polished Si_3N_4, (g, h) PEEK, 600 grit, (j, k) PEEK, 2000 grit, (m, n) Ti6Al4V 600 grit and (p, q) Ti6Al4V 2000 grit. EDX spectra of (c) as-fired Si_3N_4, (f) polished Si_3N_4, (i) PEEK, 600 grit, (l) PEEK, 2000 grit, (o) Ti6Al4V 600 grit and (r) Ti6Al4V 2000 grit, after 7 days in α-MEM

Author Manuscript Author Manuscript Author Manuscript Author Manuscript

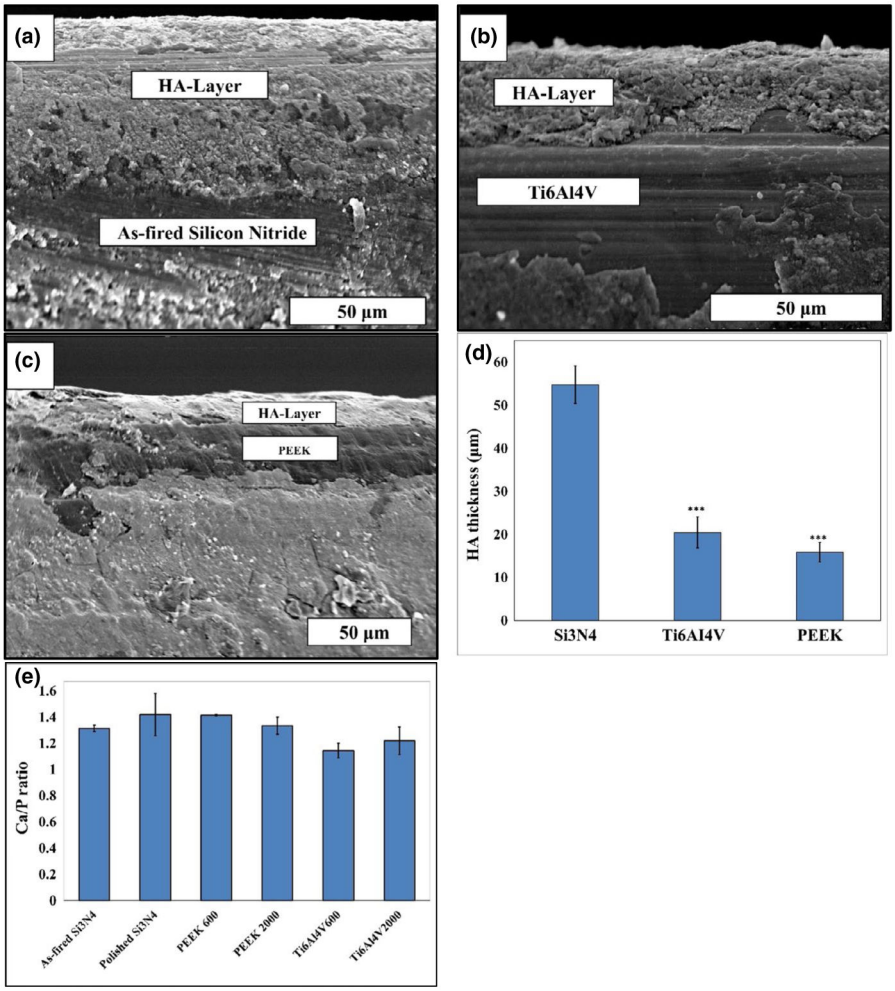

FIGURE 6.

SEM images show the interface between the formed HA layer and the (a) as-fired Si_3N_4, (b) Ti6Al4V 600 grit and (c) PEEK 600 grit samples surfaces, (e) HA-Layer thickness (µm), and Ca/P ratio with standard deviation bar, calculated from the EDS data

Author Manuscript Author Manuscript Author Manuscript Author Manuscript

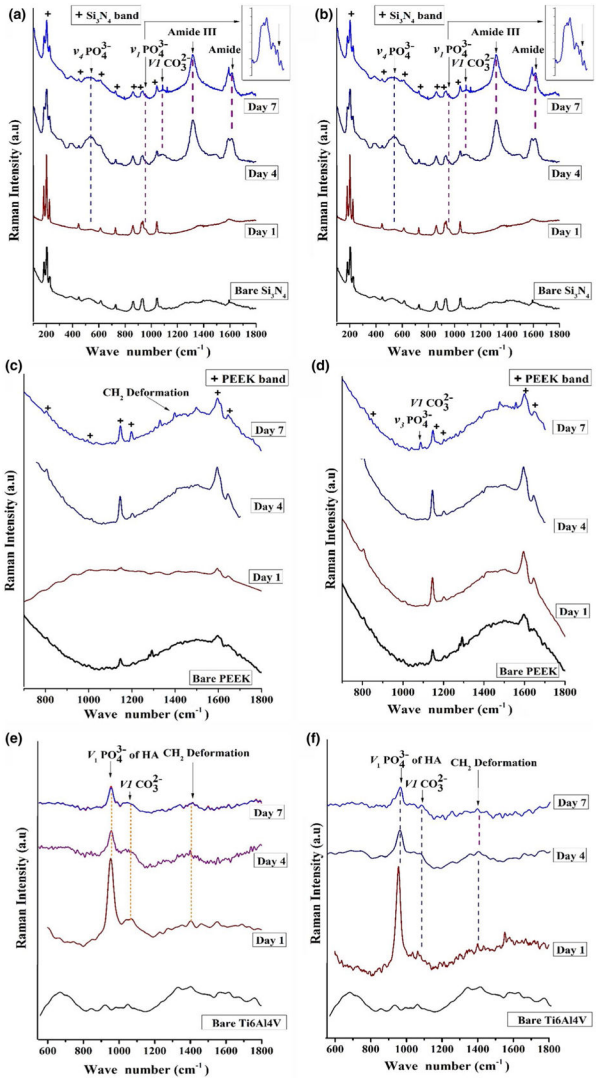

FIGURE 7.

Raman Spectroscopic graphs for the bare and the immersed samples surfaces (1, 4 and 7 days) of (a) as-fired Si_3N_4, (b) polished Si_3N_4, (c) PEEK, 600 grit, (d) PEEK, 2000 grit, (e) Ti6Al4V 600 grit and (f) Ti6Al4V 2000 grit

Author Manuscript Author Manuscript Author Manuscript Author Manuscript

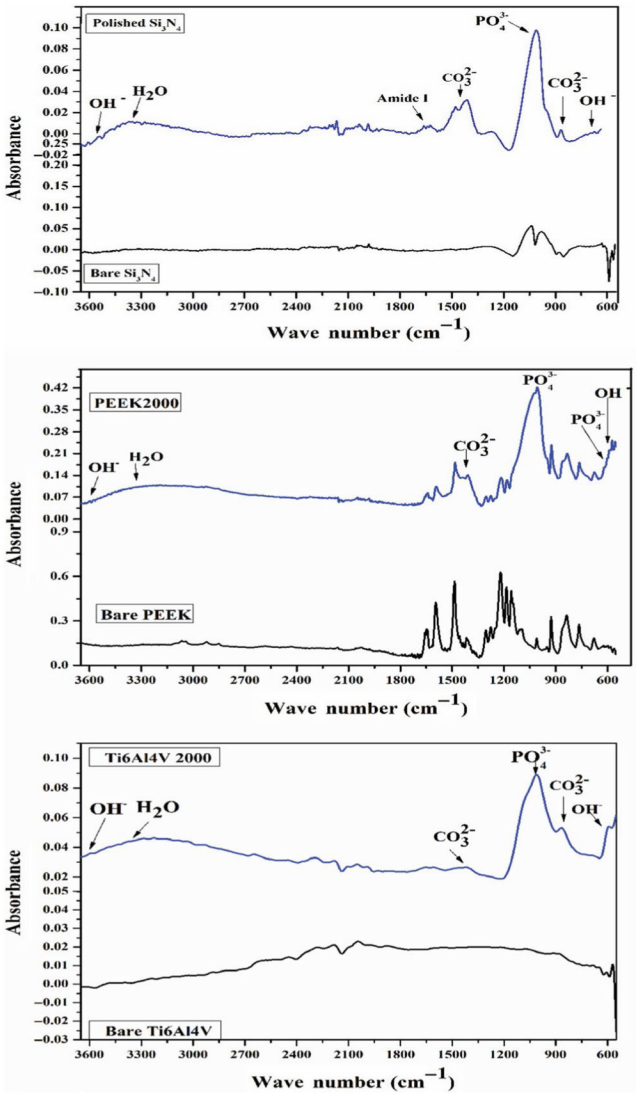

FIGURE 8.

FT-IR spectrum of HA formation on the surface of polished Si_3N_4, PEEK, 2000 grit and Ti6Al4V 2000 grit

Author Manuscript Author Manuscript Author Manuscript Author Manuscript

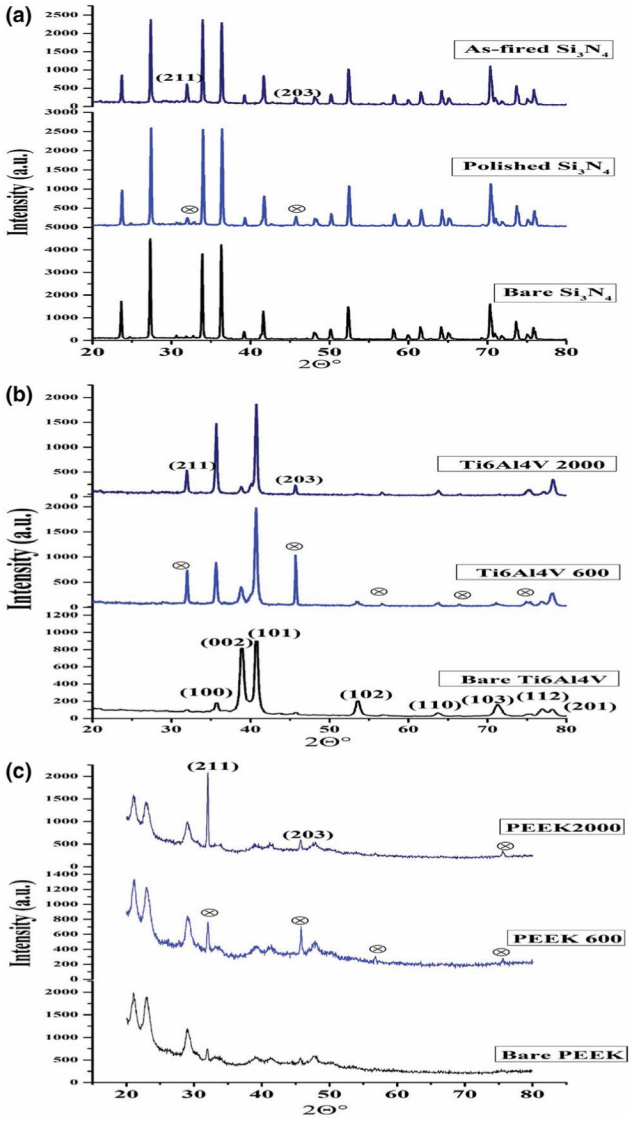

FIGURE 9.

XRD results for (a) bare Si_3N_4, polished Si_3N_4 + HA and as-fired Si_3N_4 + HA; (b) bare Ti6Al4V alloy, Ti6Al4V 600 grit + HA and Ti6Al4V 2000 grit + HA; (c) bare PEEK, PEEK 600 grit + HA and PEEK 2000 grit + HA

Author Manuscript Author Manuscript Author Manuscript Author Manuscript

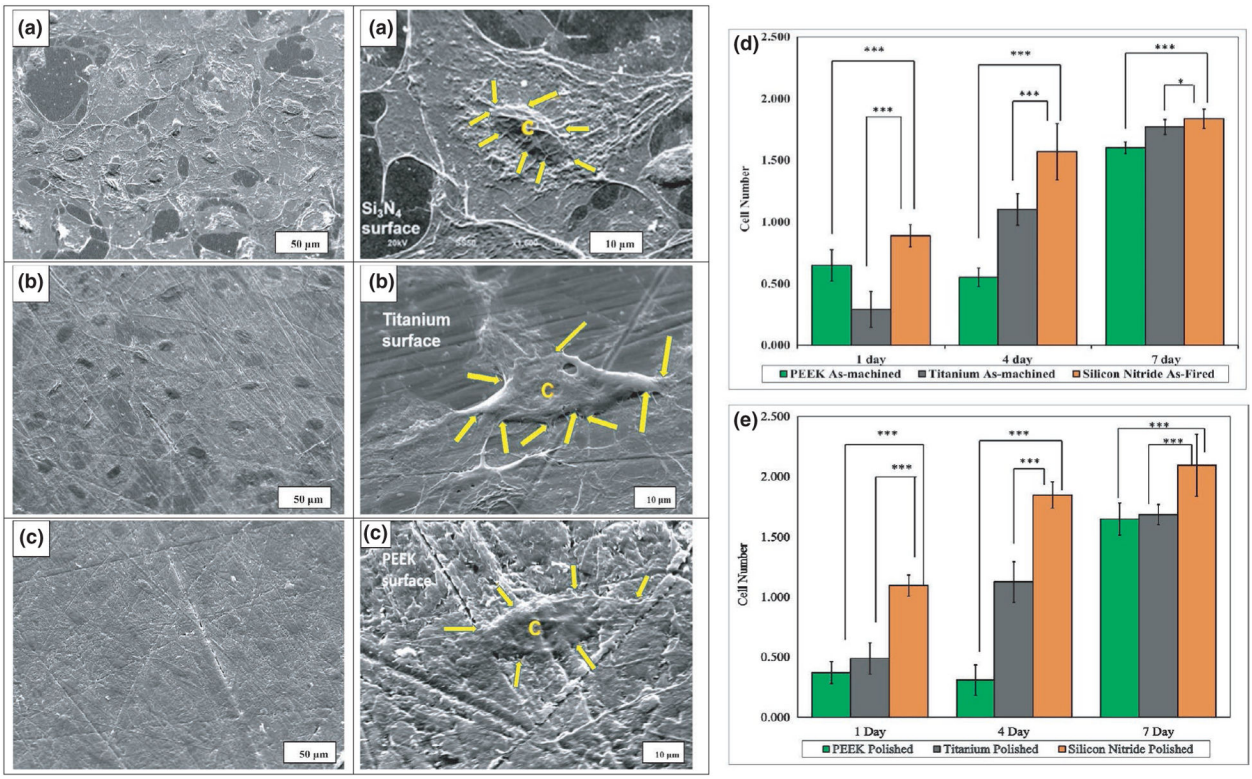

FIGURE 10.

SEM images of cell adhesion on (a) silicon nitride (as-fired), (b) Ti6Al4V (as-machined) and (c) PEEK (as-machined), C represents the cell and yellow arrows shows the filopodia on these surfaces, (d) and (e) represent cell proliferation (MTS assay) with MC3T3-E1 cells; (d) shows as-machined PEEK, Ti6Al4V and as-fired Si_3N_4, (e) shows polished samples of PEEK, Ti6Al4V and Si_3N_4

Author Manuscript Author Manuscript Author Manuscript Author Manuscript

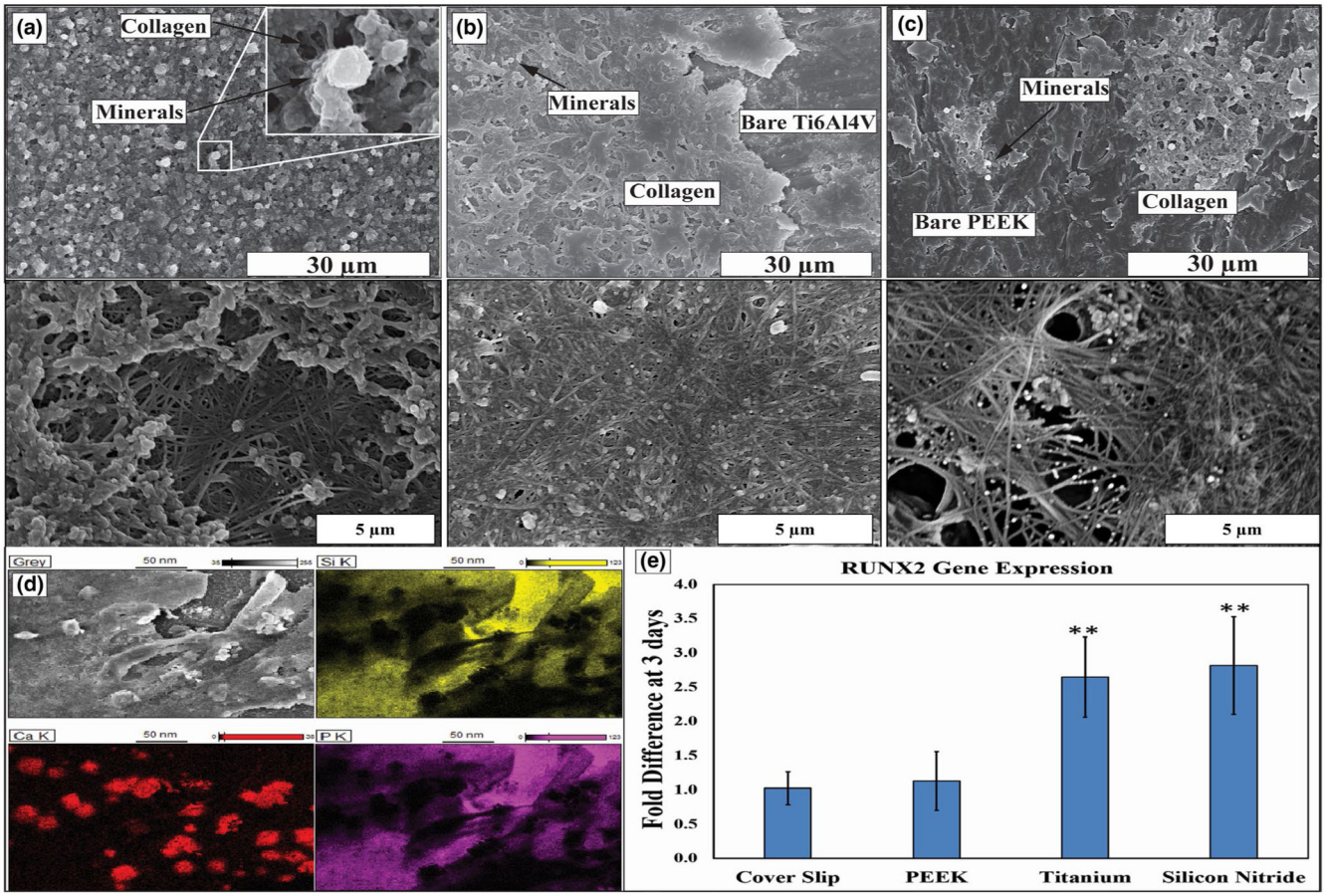

FIGURE 11.

HR-SEM images at different magnifications showing the matrix deposition after 30 days of the in vitro study on (a) silicon nitride (as-fired), (b) Ti6Al4V (as-machined) and (c) PEEK (as-machined), (d) EDX mapping represents the matrix deposition on the as-fired Si_3N_4 surface, (e) graph indicates the RUNX2 gene expression on PEEK, Ti6Al4V and Si_3N_4 surfaces compared to glass coverslip as a control after 3 days of the in vitro study, with standard deviation bar

Author Manuscript Author Manuscript Author Manuscript Author Manuscript

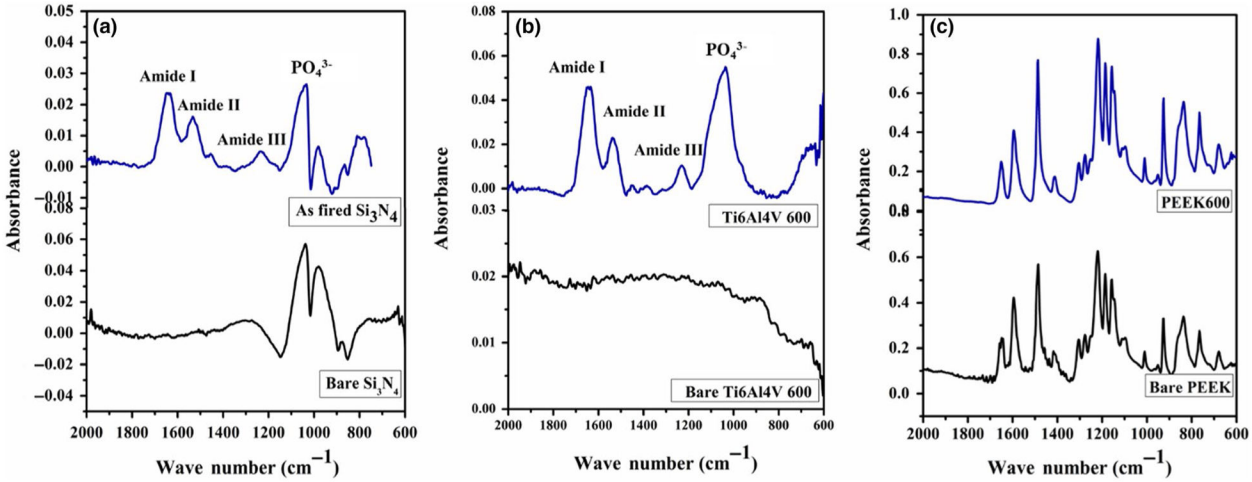

FIGURE 12.

Represents the FT-IR spectra of the matrix deposition after 30 days of the in vitro study on (a) silicon nitride (as-fired), (b) Ti6Al4V (as-machined) and (c) PEEK (as-machined)

Author Manuscript Author Manuscript Author Manuscript Author Manuscript

TABLE 1

Summary of the AFM, optical profilometer and KLA Tencor roughness parameters; (R_a) roughness average and (R_q) the root-mean-square roughness of all samples

	AFM		Optical profilometer		Stylus profilometer		AFM (HA deposition)	
Data	R_a (nm)	R_q (nm)	R_a (nm)	R_q (nm)	R_a (nm)	R_q (nm)	R_a (nm)	R_q (nm)
Sample								
As-fired Si_3N_4	241	305	309	399	140	180	438	555
Polished Si_3N_4	31	36	9	13	4	6	561	702
PEEK 600 grit	295	357	496	619	122	155	405	508
PEEK 2000 grit	144	172	164	206	52	64	458	523
Ti6Al4V600 grit	135	166	140	183	38	53	226	300
Ti6Al4V2000 grit	64	83	89	120	17	24	429	563

Med Devices Sens. Author manuscript; available in PMC 2022 July 01.